University of Jyväskylä

Department of Physics

Masters Thesis

Optical properties of small, spherical sodium clusters and dimers calculated using the jellium model and lr-TDDFT

Author:
Elli Selenius

Instructors:
Hannu Häkkinen,
Sami Malola,
Lauri Lehtovaara

12.1.2016

ABSTRACT

The birth of the localized surface plasmon resonance (LSPR) in spherical jellium clusters was investigated using the linear response time-dependent density functional theory (lr-TDDFT) and the program package GPAW. Systems of two spherical jellium clusters were also studied to see how the optical absorption spectrum changes when the separation between the clusters changes. The studied systems were spherical jellium clusters with 40, 58, 92, and 138 electrons, and systems of two spherical 8-electron jellium clusters with separations ranging from zero to four times the length of the radius of the clusters. The systems of two spheres were compared to a system with only one 8-electron jellium sphere. A 138-electron jellium cluster in the shape of a cuboctahedron was also studied to see how the lifting of the spherical symmetry affects the optical spectrum. All the studied clusters had the density of sodium.

The largest absorption peaks were also studied using the time-dependent density functional perturbation theory (TD-DFPT). The single-electron transitions contributing to these peaks were analysed using transition contribution mapping (TCM). The electron density fluctuations caused by these transitions, i.e. the induced densities, were also analysed.

All the studied systems were found to have absorption peaks caused by collective transitions. The cluster with 40 electrons had two large peaks, which can be understood as a split plasmon peak. The 58-electron, 92-electron, and 138-electron clusters had a single, large absorption peak caused by a collective transition. Most the induced density for these peaks was concentrated on the surface of the jellium spheres. Thus, these peaks have all the properties of a LSPR peak. The absorption spectra for these clusters were similar to those from earlier jellium studies.

The effect of the shape of the cluster was studied by comparing the optical properties of the two 138-electron clusters, a sphere and a cuboctahedron. The optical spectra, TCM figures and induced densities of these two clusters differed noticeably from each other. , In the systems with two 8-electron clusters, the shape of the absorption spectrum differed significantly from the spectrum of a single sphere only for separations of less than 1.5 times the radius. The intensity and location of the largest absorption peak were dependent on the separation also for larger separations. The energy of the largest peak got first smaller and then bigger when the separation between the clusters got bigger, like in an earlier jellium study. However, the separation at which the energy of the peak was at minimum was larger in this study than in the earlier study, where bigger and denser jellium clusters were used.

Keywords: jellium cluster, sodium cluster, dimer, optical properties, absorption spectrum, plasmon, TCM, GPAW, TDDFT

,

TIIVISTELMÄ

Lokalisoituneen pintaplasmoniresonanssin (*localized surface plasmon resonance*, LSPR) syntyä pallomaisissa jellium klustereissa tutkittiin käyttämällä lineaarisen vasteen ajasta riippuvaa lokaalia tiheysfunktionaaliteoriaa (*linear response time-dependent density functional theory*, lr-TDDFT) ja GPAW-ohjelmaa. Myös kahden pallomaisen, kahdeksanelektronisen jellium-klusterin systeemejä tutkittiin, jotta nähtäisiin, miten optinen spektri muuttuu, kun klusterien välinen etäisyys muuttuu. Tutkittavat systeemit olivat pallomaiset jellium-klusterit, joissa oli 40, 58, 92 ja 138 elektronia, sekä kahden pallomaisen, kahdeksanelektronisen jellium-klusterin systeemit, joissa klusterien välinen etäisyys vaihteli nollasta neljä kertaa klusterien säteen mittaiseen matkaan. Kahden pallon systeemejä vertailtiin yhden kahdeksanelektronisen pallon systeemiin. Yksi tutkittava systeemi oli 138 elektronin klusteri, jonka muoto oli kuboktaedri. Tämän klusterin avulla tutkittiin, miten pallosymmetrian murtuminen vaikuttaa optiseen spektriin.

Suurimpia absorptiospektrin piikkejä analysoitiin myös käyttämällä ajasta riippuvaa tiheysfunktionaalista häiriöteoriaa (*time-dependent density functional perturbation theory*, TD-DFPT). Yksihiukkasiirtymiä, jotka aiheuttavat kyseiset piikit, tutkittiin käyttäen TCM-analyysiä (*transition contribution mapping*), jonka avulla absorptiopiikkiin vaikuttavien elektronien siirtymien kontribuutioita voidaan tarkastella. Näiden siirtymien aiheuttamia elektronitiheyden fluktuaatioita eli indusoituja tiheyksiä analysoitiin myös.

Kaikista tutkituista systeemeistä löytyi kollektiivisten siirtymien aiheuttamia absorptiopiikkejä. 40-elektronisen klusterin spektrissä oli kaksi suurta piikkiä, jotka voidaan ymmärtää jakautuneena plasmonipiikkinä. 58-, 92- ja 138-elektronisten klusterien spektreissä oli yksi suuri piikki, joka aiheutui kollektiivisesta elektronien virittymisestä. Näitä piikkejä vastaavista indusoiduista tiheyksistä suurin osa sijaitsi klusterien pinnalla. Näillä absorptiopiikeillä on siis kaikki LSPR-piikin ominaisuudet. Tutkittujen klusterien absorptiospektrit muistuttivat aiemissa jellium-tutkimuksissa saatuja spektrejä.

Klusterin muodon vaikutusta tutkittiin vertaamalle kahden 138-elektronisen klusterin, pallon ja kuboktaedrin, optisia ominaisuuksia toisiinsa. Näiden kahden klusterin optiset spektrit, TCM-kuvat sekä indusoidut tiheydet poikkesivat toisistaan selvästi.

Kahden kahdeksanelektronisen klusterin systeemeissä absorptiospektrin muoto poikkesi selvästi yksittäisen klusterin absorptiospektristä vain, kun klusterien etäisyys toisistaan oli alle puolitoista kertaa klusterien säteen verran. Suurimman absorptiopiikin intensiteetti ja paikka kuitenkin riippuivat klusterien välisestä etäisyydestä myös suurempien etäisyyksien tapauksessa. Suurimman absorptiopiikin energia ensin pieneni ja sitten suureni klusterien välimatkan kasvaessa kuten aiemmassa jellium-tutkimuksessa. Etäisyys, jolla absorptiopiikin energia oli pienimmillään, oli kuitenkin tässä tutkimuksessa suurempi kuin aiemmassa, jossa käytettiin suurempia ja tiheämpiä jellium-klustereita.

Avainsanat: jellium-klusteri, natriumklusteri, dimeeri, optiset ominaisuudet, absoprtiospektri, plasmoni, TCM, GPAW, TDDFT

CONTENTS

1 INTRODUCTION

Metal particles that are are smaller than the wavelength of visible light have optical properties that are very different from those of larger particles. Small metal colloids have been used in the making of coloured glass since the time of the Romans. For example, colloidal gold particles of a certain size can make glass red in small concentrations. A striking example of the effect of noble metal nanoparticles is the Lycurgus cup, which was made in the 4th century in the empire of Rome. It is made of glass and it contains gold-silver alloy nanoparticles, which cause it to appear red when viewed in light transmitted trough the glass and greenish when viewed in reflected light [1]. Later, small noble metal particles have been used to produce colors in stained-class windows, for example in the rose window of Notre-Dame Cathedral. However, the optical properties of small metal particles were not systematically examined before Michael Faraday, who published his study of the different colours caused by colloidal gold particles in 1857 [2]. First calculation methods for the optical properties of these metal clusters were developed in 1908 by Gustav Mie [3].

The phenomenon that makes small metal clusters optically so interesting is the surface plasmon resonance (SPR). Surface plasmon resonance is the result of a collective excitation of the valence electrons in metal, and it is manifested as a tall peak or peaks in the optical absorption spectrum of a metal particle. In small clusters with lengths less than the wavelength of incident electromagnetic radiation, the surface plasmons do not propagate, and the phenomenon is called the localized surface plasmon resonance (LSPR). Because the absorption spectrum is dependent on the material [3], shape [4], [5], and size [6] of the cluster, the surface plasmon resonance can be tuned by changing these properties.

When two metal nanoparticles are placed next to each other, their surface plasmons couple, and the resonance frequency of this coupled LSPR depends on the separation between the particles [7]. This dependence on the separation makes it possible to determine the distance between two silver or gold nanoparticles by comparing the optical spectra to known experimental or theoretical results. If metal nanoparticles are attached to the ends of a biomolecule, this 'plasmon ruler' can be used to determine the length of the biomolecule, such as a DNA strand [8]. The dielectric environment of the clusters also has an effect on the position of the LSPR peak [9]. This property can be used in localized surface plasmon resonance sensing, where arrays of nanoparticles are used in detecting molecules attached to these particles [10].

Arrays of silver or gold nanoclusters can be used for other sensing methods as well. An external electromagnetic field can be greatly enhanced in the junction between metallic nanoparticles due to the plasmonic coupling [12]. This leads to surface-enhanced Raman scattering (SERS): the intensity of the Raman spectrum of molecules on surfaces made of metal nanoparticles is much stronger than the Raman spectrum of isolated molecules [11]. The strength of the enhancement depends on the arrangement and shape of the nanoparticles.

Noble metal nanoparticles are also suitable for medicinal applications, because of their low

toxicity. For example, gold nanoparticles can be used in cancer treatment in imaging and photothermal cancer therapy. When antibody-conjugated nanoparticles bind to different cells, their SPR frequency changes according to the nature of the cells. This enables the differentiation of cancer cells from noncancerous cells [13]. In photothermal cancer therapy noble metal nanoparticles are conjugated so that they bind to cancer cells. When the cells are then exposed to laser radiation at a frequency close to the plasmon frequency of the nanoparticles, the strong photoabsorption of the nanoparticles causes the photothermal death of the cancer cells [14]. Nanoshell clusters and nanorods are often used in these applications because their optical response can be tuned by changing the shell thickness in the case of the nanoshell or the aspect ratio in the case of the rods [13].

In this study the optical spectra of small sodium clusters are investigated using the jellium model and the program package GPAW [15], [16]. The density functional theory (DFT) is used in the calculations, and the absorption spectra are calculated using linear response time-dependent DFT (lr-TDDFT). The transitions contributing to the largest absorption peaks are analysed using transition contribution mapping (TCM) [17]. The induced densities caused by these transitions are also analysed. The aim is to study the birth of the surface plasmon resonance and the single-electron transitions contributing to it in very simple systems, spherical jellium Na clusters. Sodium was chosen because the homogeneous jellium model is well suited for modelling alkali metals, such as sodium [18].

The systems studied are isolated jellium spheres with 20, 40, 58, 92, and 138 electrons, and systems of two small 8-electron jellium spheres with different separations between the spheres. A cluster in the shape of a cuboctahedron with 138 electrons is also studied. All these clusters are in vacuum. For the single spherical clusters, the evolution of the surface plasmon with increasing cluster size is studied. The induced density caused by some of the single-electron transitions contributing to the plasmon peaks are also studied separately. The results for the cuboctahedron are compared to those for the spherical cluster with the same amount of electrons to see the effect the breaking of the spherical symmetry has on the optical properties.

As noted above, systems of two or more metal clusters are used in many applications. Here, the effect of the separation on the optical spectra, especially the shape, size and location of the largest absorption peak, is studied in the case of two small jellium clusters. The evolution of the single-electron transitions and the induced densities are also studied.

The spectra obtained for the spherical clusters and the systems of two spherical clusters were also compared to previous jellium studies to see if the trends were similar.

2 THEORY

Surface plasmon resonance can be observed in systems with multiple free electrons: the smallest clusters with only a couple atoms have a molecule-like optical spectrum with peaks that result from individual single-electron transitions [19]. However, absorption peaks that seem to be caused by collective excitations have been measured for sodium clusters with as few as six atoms [6].

2.1 Calculation methods for the absorption spectrum

Classically, a plasmon can be treated as a collective oscillation of free electrons around the positive ion core caused by an external electromagnetic field. In the case of the surface plasmon, this oscillation happens at the surface of the material. The oscillating electric field causes a displacement of the free electrons relative to the ion core. The ion core then exerts a restoring force on the displaced electrons. At a certain resonance frequency there is a large peak in the optical absorption spectrum of the particle: this is the SPR peak.

Gustav Mie developed a method to calculate the optical absorption spectrum for small spherical metal clusters using the Maxwell equations in 1908 [3]. For spherical clusters, there are exact solutions to the Maxwell equations. The optical spectrum depends on the the material of the cluster via the dielectric function of the metal, and also on the size of the cluster. In this classical Mie theory there is only one surface plasmon peak in the optical spectrum of a cluster.

If the particles are sufficiently small compared to the wavelength of the electromagnetic radiation, the electric field can be approximated as constant. This is the quasistatistic approach [9]. However, using the quasistatistic approach and the bulk dielectric function of the metal, the expression for the resonance frequency of a cluster does not depend on the size of the cluster [19]. Since various experiments show the plasmon frequency to be size-dependent, other forms than the bulk expression are often used for the dielectric function. For example, the dielectric function can be expressed using the Drude model. In the hydrodynamic Drude model the free valence electrons are treated as charged fluid and their motion is studied using hydrodynamic equations [20].

As there are exact solutions for the Maxwell equations only for some highly symmetric shapes, other methods based on the Maxwell equations have been developed for metal clusters. One of these is the discrete dipole approximation (DDA) [21], which can be used for clusters of any shape. There the cluster is divided into many cubical elements, which are so small that only dipole interactions need to be taken into account inside each element. In addition to the interaction of an element with the external field, the interactions with the induced fields in the other elements must be included in the calculations. Another method is the finite difference time domain method (FDTD) [22]. Here the calculations are performed on a grid, and the differential Maxwell equations are changed into finite-difference equations.

There are also models that incorporate some aspects of quantum mechanical (QM) cal-

culations into the classical framework. For example, in the quantum-corrected (QC) model [23] for calculating plasmons in systems of two nanoparticles close to each other, electron tunnelling between the two particles is modelled by a fictitious conductive material between the nanoparticles. Now the Drude model can be used, with a separation-dependent dielectric function that can be obtained from QM calculations.

One approach for complex shapes is the hybridization model [24] where the plasmon in a cluster of a complex shape is understood as hybridization of the plasmons for the more simple shapes the cluster is made of. This approach can be used e.g. for many-layer nanoshells [24] and dimers [25].

In QM calculations, the time-dependent density functional theory (TDDFT) [26] is often used used for the calculation of optical properties. For example, the local density approximation (LDA) [27] with the random-phase approximation (RPA) has been used in many studies of plasmons in metal clusters [28], [29], [30].

The self-consistent jellium model [31] is often used with TDDFT in the calculation of the optical properties of metal clusters or nanoparticles of different shapes, such as spheres [28], nanowires[32], or nanoshells [33]. In the jellium model only the valence electrons of the atoms are treated explicitly: the other electrons together with the positive cores of the atoms are treated as usually homogeneous positive background density. This makes the jellium models quite simple and suitable also for the calculation of large systems, since it is not computationally heavy.

The homogeneous jellium model is obviously not as accurate as full atomic calculations, but it does reproduce the trends in the optical spectrum of metal clusters compared to experimental results [29], [28] or atomic calculations [34]. In the homogeneous jellium model the edge of the positive charge density is sharp. Other than homogeneous jellium models have been developed: the ionic structure has been mimicked for example by making the positive jellium density spherically symmetric but centrally compressed [35]. In the ultimate jellium mode [36] no restrictions are given to the shape and density of the positive jellium background during the ground state calculation. One drawback of all the jellium models is that they are not suitable to modelling ligand-covered clusters [19].

2.2 Tunability of the plasmon resonance

The shape of the clusters or nanoparticles has a considerable influence on the surface plasmon resonance frequency, and clusters of different shapes but same material can be identified based on their optical response [4], [37]. Also the size of the particle influences the resonance wavelength: for sodium clusters, the SPR energy experiences a red shift as the size of the clusters gets smaller. This is due to the spill-out of electrons, relatively greater for small clusters than for large clusters, which causes the effective electron density to get smaller as the size of the cluster gets smaller [6].

The shape of the cluster has other effects on the surface plasmon than just the shifting of the resonance frequency: deformations from the spherical shape can cause splitting of the resonance peak. This causes for example deformed open-shell sodium clusters to have multiple resonance peaks [38], [36]. Spherical clusters can also have split plasmon peaks: closed-shell spherical sodium clusters with 20 and 40 atoms have also been reported to have split plasmons [39], [6]. This splitting can be explained by the coupling of unperturbed single particle-hole transitions, that are close in energy to the SPR peak, to the surface

plasmon [40], [41].

In systems of two or more clusters, the distance between the clusters also influences the energy and sometimes also the shape of the plasmon peak. Plasmonic coupling between two adjacent nanoparticles is of great interest because of the applications mentioned in the introduction. The effect of the separation between two nanoparticles to the plasmon peak have been studied for example for spherical particles [30], infinitely long nanowires [32], and nanorings [42]. In the case of non-isotropic particles, such as nanorods [43], the orientation of the particles is also of interest.

2.3 Models and approximations used

Here the simple homogeneous jellium model together with TDDFT was used in the calculations. The calculations were performed with GPAW, which is a program package for the Atomic Simulation Environment (ASE) [44]. In GPAW the calculations are performed on a real-space grid using the projector augmented wave (PAW) [45] method. Because the clusters studied were spherical or close to a spherical shape, an YLM analysis was performed on the clusters, where the Kohn-Sham states were projected into spherical harmonics. The projected density of states (PDOS) could then be plotted using different colours for the different angular momentum character of the states. The different type of states were named using the convention for atomic orbitals.

The optical spectra were calculated with linear response TDDFT (lr-TDDFT) with the Casida formalism as implemented in GPAW [46]. When the optical spectra had been calculated, some absorption peaks were studied using the time-dependent density functional perturbation theory (TD-DFPT) [47]. The individual single-electron transitions contributing to the peak and the magnitude of their absorption coefficients were obtained. TCM figures were then plotted for the studied peaks. In a TCM figure the x axis depicts the energy of the initial Kohn-Sham state of an electron, the y axis the energy of the final Kohn-Sham state where the electron is excited to, and the squared magnitude of the absorption coefficient for each transition is shown as the brightness of the contribution. The TCM analysis was combined with the YLM analysis, so that the type of the initial and final states are also shown in the TCM figure. The induced densities showing the dipole oscillation caused by all the transitions contributing to the studied peak were also calculated with TD-DFPT and visualized with the molecular graphics program VMD [48].

The theory behind the used approximations and techniques is described in more detail in the theory section of a previous study [49].

3 RESULTS

3.1 Spherical clusters with 40, 58, 92, and 138 atoms

The optical properties of four jellium clusters with the density of sodium and with 40, 58, 92, and 138 valence electrons were studied. These clusters were chosen because they are so-called magic clusters: they all have full electron shells, so according to the jellium model they are spherical. The grid spacing was 0.4 Å for all sizes. The sizes of the cubic unit cells were chosen so that there was at least 8 Å of vacuum between the jellium edge of the cluster and the edge of the unit cell. The energy cut-off in the calculation of the optical spectra was 6 eV for the cluster with 138 electrons and 7 eV for all the other sizes. This means that all states within 7 eV (6 eV in the case of Na_{138}) of the energy of the highest occupied molecular orbital (HOMO) were included in the calculation.

3.1.1 Spherical jellium cluster Na_{40}

The radius of the Na_{40} cluster was 7.11 Å and the side length of the calculation box was 31 Å. The projected density of states and the optical absorption spectrum for the cluster can be seen in figure 1. The HOMO state is the 2p state and the lowest unoccupied molecular orbital (LUMO) state is the 1g state. The energy gap between these two states, the HOMO-LUMO gap, is quite small for this system, as can be seen from figure 1a. The density of the states is almost continuous after about 3 eV.

The 621 lowest states were included in the lr-TDDFT calculation. A small peak, caused probably by a molecular single-electron transition, is seen at about 1 eV in figure 1b. There are two larger peaks at 2.54 eV and 3.00 eV. These two peaks were further analysed.

The TCM plots of the two large peaks can be seen in figure 2. For both peaks, there are contributions from transitions 2p→3d, 1f→1g, 1f→2d, 1f→3d, and 1f→2g. For the larger of these peaks there are also contributions from transitions 2s→3p, 2p→1d, 1d→2f, 1d→2p, and a transition from 2p to a state near 3.3 eV, where the density of states is

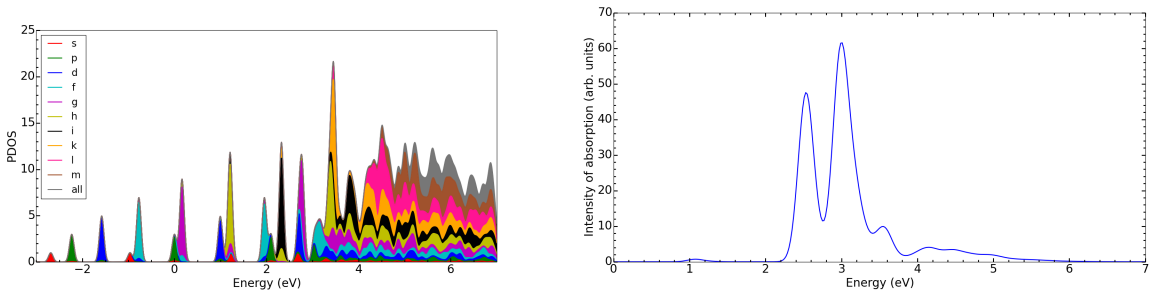

(a) PDOS **(b)** spectrum

Figure 1: The projected density of states and the optical absorption spectrum for the Na_{40} jellium cluster. The HOMO level has been set to zero in the PDOS figure. The width of the Gaussian broadening used for the states in figure 1a was 0.05 eV and the width of the Gaussian used for the spectrum in figure 1b was 0.1 eV.

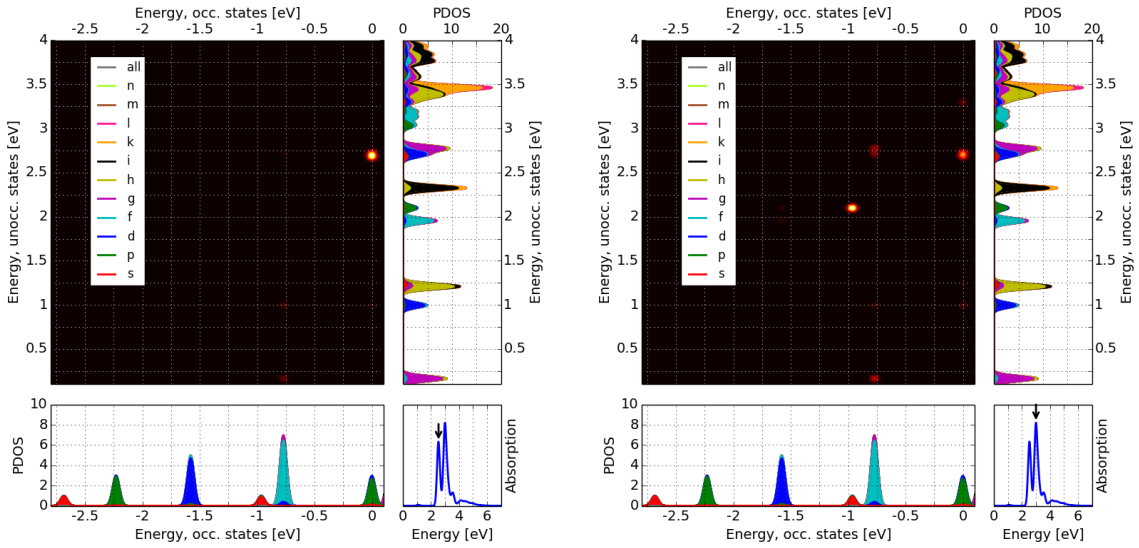

(a) 2.54 eV **(b)** 3.00 eV

Figure 2: The TCM figures for the two largest peaks for the Na_{40} jellium cluster. The occupied Kohn-Sham states are shown in the lowest subplot and the unoccupied Kohn-Sham states in the subplot on the right. The single-electron transitions from an occupied state to an unoccupied state are plotted with a colour ranging from red to bright yellow. The brightness of the colour corresponds to the strength of the contribution of this transition. In the PDOS figures the HOMO level is set to zero, and the width of the Gaussian distribution used for the states is 0.03 eV. The contributions have been widened with a Gaussian with a width of 0.025 eV in both x and y directions.

already quite continuous. For the smaller peak at 2.54 eV the contribution from transition 2p→3d is much stronger than the other contributions. For the larger peak, at 3.00 eV, the strongest contribution comes from the transition 2s→3p, but the contribution from 2p→3d is also quite strong. All in all, the largest peak is caused by a much more collective transition than the second largest peak.

The induced densities for the largest peaks can be seen in figure 3. For both peaks, there are several shells of induced density caused by dipole oscillations. There are also some oscillations in the opposite direction than the main dipole oscillation.

In figure 4 the induced densities from figure 3 are plotted radially along the x axis. The

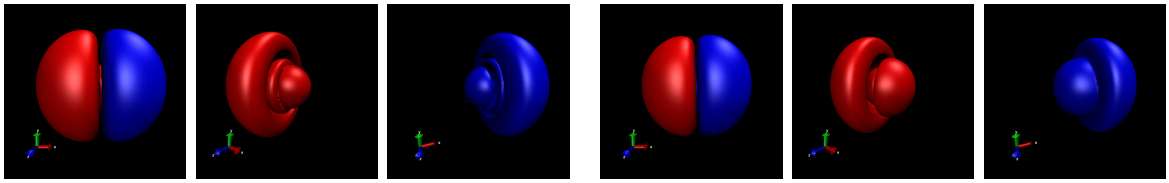

(a) 2.54 eV **(b)** 2.54 eV, positive part **(c)** 2.54 eV, negative part **(d)** 3.00 eV **(e)** 3.00 eV, positive part **(f)** 3.00 eV, negative part

Figure 3: Induced densities for the two largest peaks of the Na_{40} jellium cluster. The isosurface values used are the positive jellium density and its negative. The positive density is shown in red and the negative in blue. In figures 3a and 3d are shown both the positive and negative parts, in figures 3b and 3e only the positive and in 3c and 3f only the negative parts. Note that figures showing only the negative or positive parts are shown from different angles than the figures showing both parts. All the figures are in the same length scale. The images have been made with VMD.

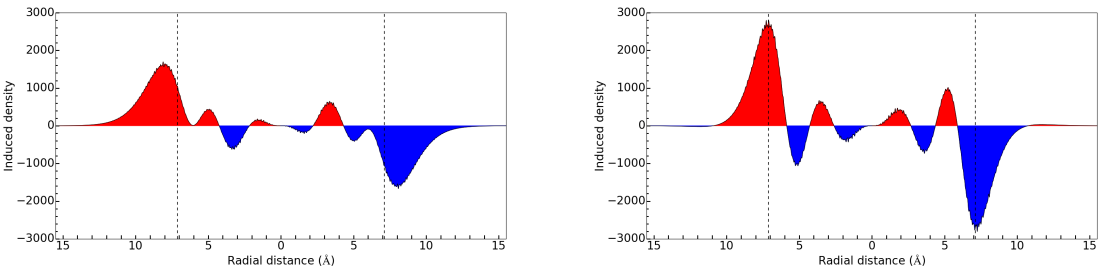

(a) 2.54 eV **(b)** 3.00 eV

Figure 4: The induced densities from figure 3 plotted radially along the x axis. The dashed lines indicate the jellium edges of the cluster.

inner shells can better be seen in this figure. There are four shells of both negative and positive induced density for both peaks, but the order of these shells is different for the two clusters. The peak density is bigger for the larger peak at 3.00 eV. For the smaller peak at 2.54 eV, more of the induced density is outside the cluster than for the larger peak. However, for both clusters, most of the induced density is concentrated near the surface, even though there are smaller oscillations inside the cluster.

3.1.2 Spherical cluster Na_{58}

The radius of the jellium cluster with 58 electrons was approximately 8.05 Å and the side length of the unit cell was 33 Å. The PDOS and the optical absorption spectrum can be seen in figure 5. From figure 5a it can be seen that the HOMO-LUMO gap is large for this system, and that the density of the states starts to be continuous somewhere around 3 eV. The HOMO state is the 1g state and the LUMO state the 2d state.

The 699 lowest states were used in the calculation of the optical properties. Two large peaks can be seen in the optical absorption spectrum in figure 5b, but the one at 2.81 eV is significantly larger than the one at 3.26 eV. There is also a small peak between 1 and 2 eV in energy, but it can not be seen in this scale. The largest peak is significantly higher than any peak in the spectrum of the cluster with 40 electrons. The two largest peaks were analysed further.

The TCM plots of the two largest peaks can be seen in figure 6. Both peaks are the result

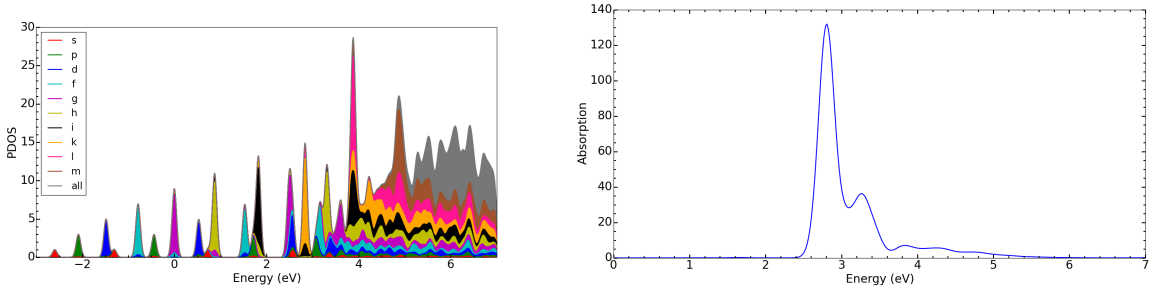

(a) PDOS **(b)** spectrum

Figure 5: The projected density of states and the optical absorption spectrum for the Na_{58} jellium cluster. The HOMO level has been set to zero in the PDOS figure. The width of the Gaussian broadening used for the states in figure 5a was 0.05 eV and the width of the Gaussian used for the spectrum in figure 5a was 0.1 eV.

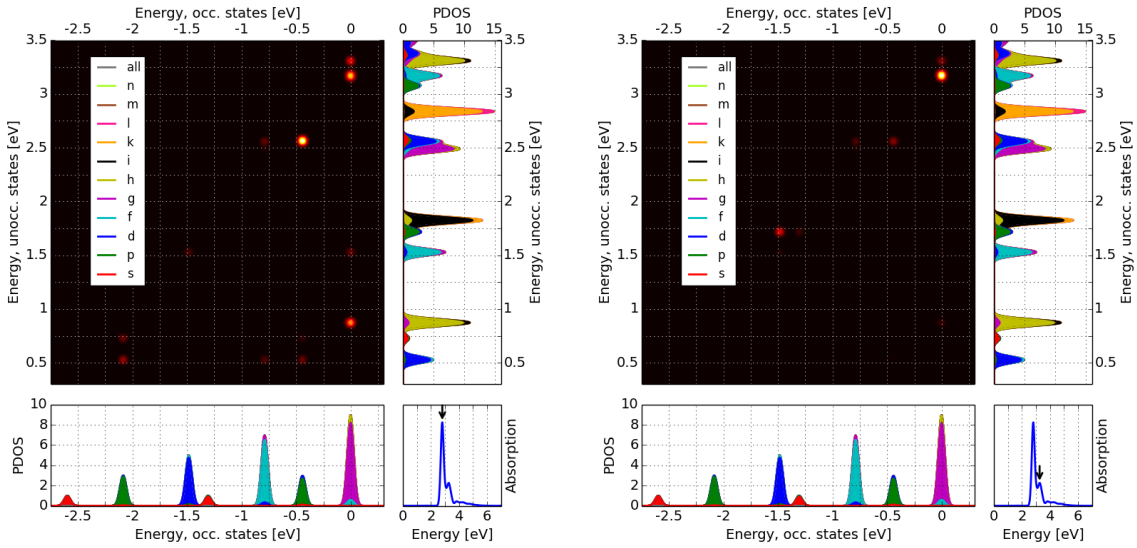

(a) 2.81 eV **(b)** 3.26 eV

Figure 6: The TCM figures for the two largest peaks for the Na_{58} jellium cluster. See details in the caption of figure 2.

of multiple transitions, the larger peak more so. Transitions contributing to both peaks are 1d→2f, 1f→3d, 2p→3d, 1g→1h, 1g→3f, and the transition from 1f to a higher state near 3.3 eV. For the first peak, the contribution from transition 2p→3d is the strongest; for the other peak, the strongest contribution comes from 1g→3f.

The second, smaller peak has also some transitions not present in the TCM for the larger peak: 1d→3p and 2s→3p. Transitions contributing to the larger peak but not to the smaller peak are 1p→2d, 1p→3s, 1f→2d, 2p→2d, 2p→3s, and 1g→2f.

In both TCM figures most of the contributions lie approximately on a diagonal belt across the figure, i.e. most of the individual transition have approximately the same excitation energy. However, especially in the TCM figure for the larger peak, there are also many transitions where the energy difference between initial and final states is significantly lower than the energy difference for the transition on the belt. These transitions lower the energy of this peak compared to the other peak.

The induced densities for the two peaks can be seen in figure 7. There is a similar shell-like structure as in the induced densities for the Na_{40} cluster, seen in figure 3. Especially the induced densities for the largest peaks, at 3.00 eV for the 40 electron cluster and at

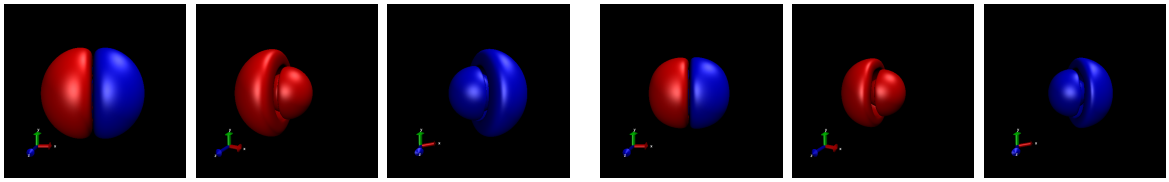

(a) 2.81 eV **(b)** 2.81 eV, positive part **(c)** 2.81 eV, negative part **(d)** 3.26 eV **(e)** 3.26 eV, positive part **(f)** 3.26 eV, negative part

Figure 7: Induced densities for the two largest peaks of the Na_{58} jellium cluster. All the figures are in the same length scale. See the caption of figure 3 for details.

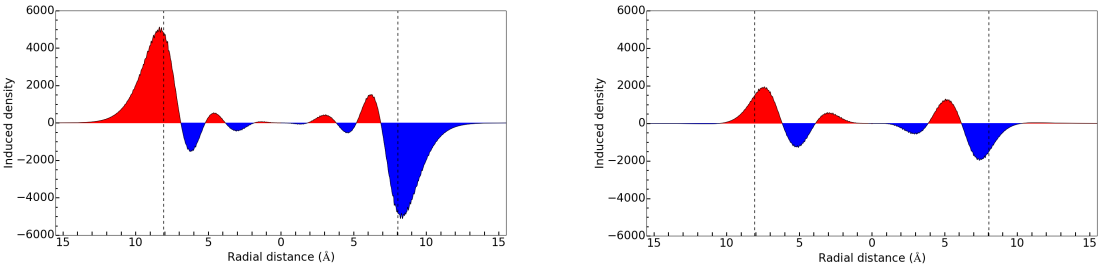

(a) 2.81 eV **(b)** 3.26 eV

Figure 8: The induced densities from figure 7 plotted radially along the x axis. The dashed lines indicate the jellium edges of the cluster.

2.81 eV for the 58 electron cluster, are similar.

The induced density from figure 7 plotted radially can be seen in figure 8. From here it can also be seen that the induced densities of the two largest peaks are very similar for the clusters with 40 and 58 electrons. Especially for the larger peak of the jellium cluster Na_{58}, at 2.81 eV, most of the induced density is concentrated on the surface of the jellium cluster. For the larger peak the highest value of the induced density is much larger than for the smaller peak.

3.1.3 Spherical cluster Na_{92}

The radius of the cluster was approximately 9.39 Å, and the side length of the unit cell was 35 Å. The 889 lowest states were included in the calculation of the optical properties. The PDOS and the optical absorption spectrum of the Na_{92} jellium cluster can be seen in figure 9. This cluster also has a clear HOMO-LUMO gap, as can be seen from figure 9a The HOMO state is the 3s state and the LUMO state the 2f state. The density of states is continuous after about 3 eV for this cluster also.

In the optical spectrum of this cluster, seen in figure 9b, there is only one larger peak, at 2.92 eV. However, a small shoulder to this peak can be seen at about 3.1–3.2 eV. There is a very small peak at just under 1 eV, although it can not be seen in the scale of figure 9b.

The TCM plot for the large peak is shown in figure 10. There are three very strong

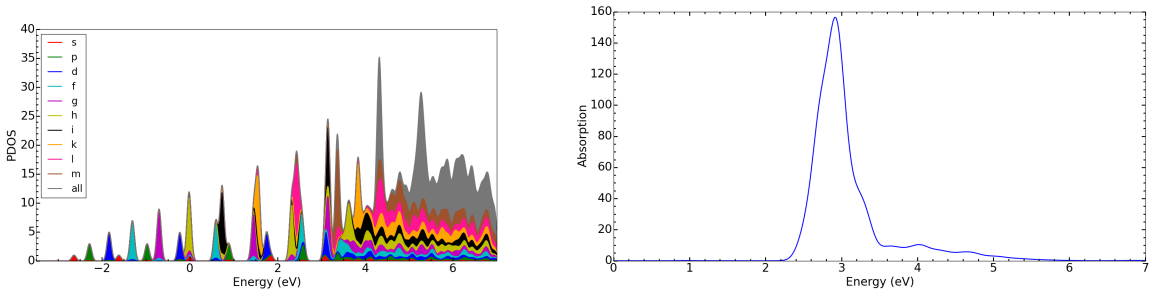

(a) PDOS **(b)** spectrum

Figure 9: The projected density of states and the optical absorption spectrum for the Na_{92} jellium cluster. The HOMO state has been set to zero in figure 9a. The width of the Gaussian broadening used for the states in figure 9a was 0.05 eV and the width of the Gaussian used for the spectrum in figure 9a was 0.1 eV.

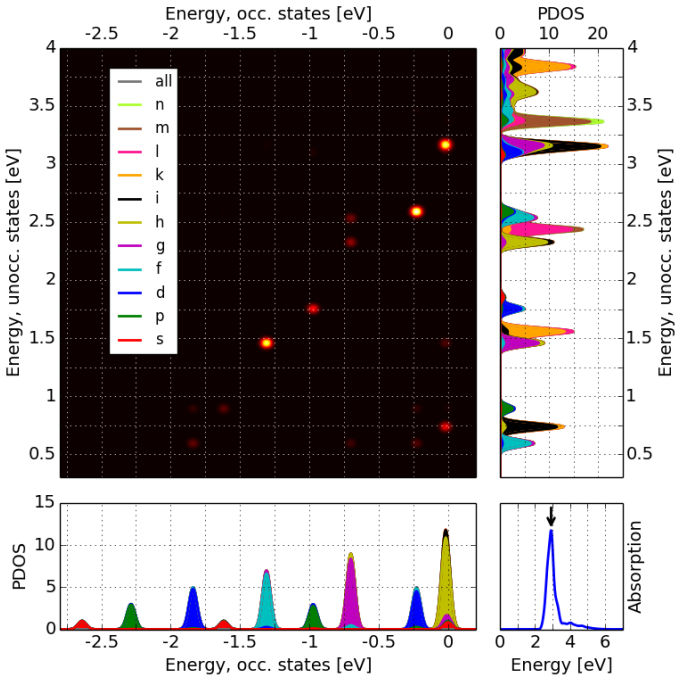

Figure 10: The TCM figure for the large peak for the Na_{92} jellium cluster. See details in the caption of figure 2.

contributions: 1f→2g, 2d→4p, and 1h→3g (also 1h→2i shows up in the same contribution as 1h→3g). Other quite strong contributions come from transitions 2p→3d and 1h→1i. These five strongest contributions were studied separately. There are 9 other contributions: 1d→2f, 1d→3p, 2s→3p, 1g→2f, 1g→2h, 1g→3f, 2d→2f, 2d→3p, and 1h→2g. Most of the transitions are again aligned roughly diagonally in figure 10, and the energy between the initial and final states is about 3 eV in these transitions. There are also some weaker transitions of lower energy.

The induced density for the peak at 2.92 eV can be seen in figure 11 and the induced density plotted radially is displayed in figure 12. The structure of the induced density is again similar to that of the induced densities of the largest peaks for the clusters with 40 and 58 electrons.

For the five strongest contributions, the induced densities were plotted separately for each contribution. The analysed contributions can be seen in figure 13. Four of them are among the diagonal transitions, one is a transition from the state before HOMO to the

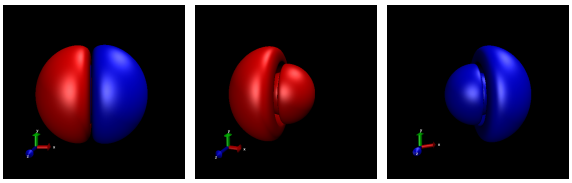

(a) pos. and neg. parts **(b)** positive part **(c)** negative part

Figure 11: Induced densitiy for the largest peak of the Na_{92} jellium cluster. All the figures are in the same length scale. See the caption of figure 3 for details.

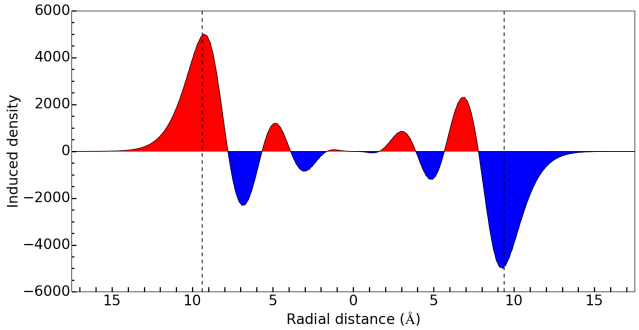

Figure 12: The induced density from figure 11 plotted radially. The dashed lines indicate the jellium edges of the cluster.

state after LUMO.

The induced densities for the contributions from figure 13 are displayed in figure 14. In figure 14 are shown these induced densities plotted radially.

The induced densities caused by different transitions have different numbers of shells. The number of the positive shells, which is also the number of the negative shells, is the principle quantum number of the molecular orbital where the electron is excited to. The transition 1h→1i, for example, causes the the electron density simply to oscillate between two ends of the sphere in the direction of the dipole moment of the electromagnetic field. Most of the overall induced density at the surface of the sphere seems to be caused by

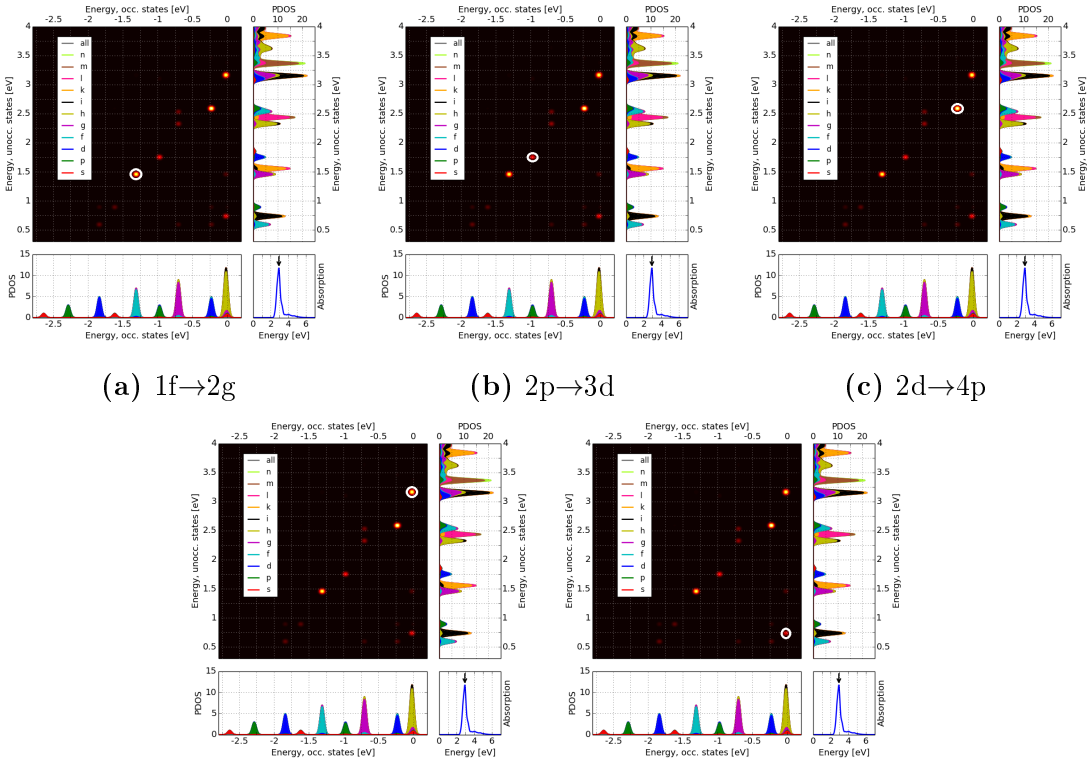

(a) 1f→2g **(b)** 2p→3d **(c)** 2d→4p

(d) 1h→3g **(e)** 1h→1i

Figure 13: The analysed transitions contributing to the largest peak in the Na_{92} jellium cluster are shown here circled in white.

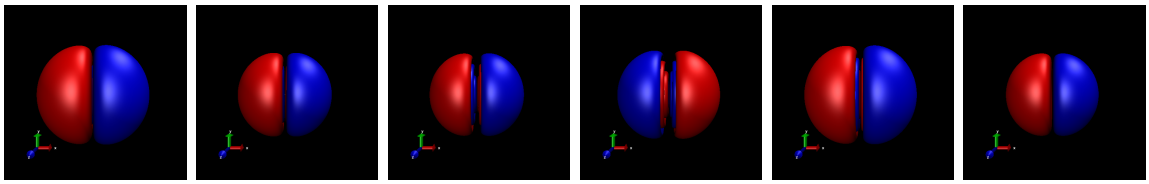

(a) all transitions **(b)** 1f→2g **(c)** 2p→3d **(d)** 2d→4p **(e)** 1h→3g **(f)** 1h→1i

Figure 14: The induced densities caused by the five strongest transitions. In figure 14a is displayed the induced density for all the transitions contributing to the largest peak. In figures 14b – 14f are the induced densities for the transitions shown in figure 13. All the figures are in the same length scale. See the caption for figure 3 for details.

this transition. The induced density of transition 2d→4p differs from the others in that the negative and positive outermost isosurface shells are on different sides of the cluster than for other transitions. This shell is also almost entirely outside the positive jellium background. This is the case also for the transition 1h→3g, which spreads the overall induced density outwards.

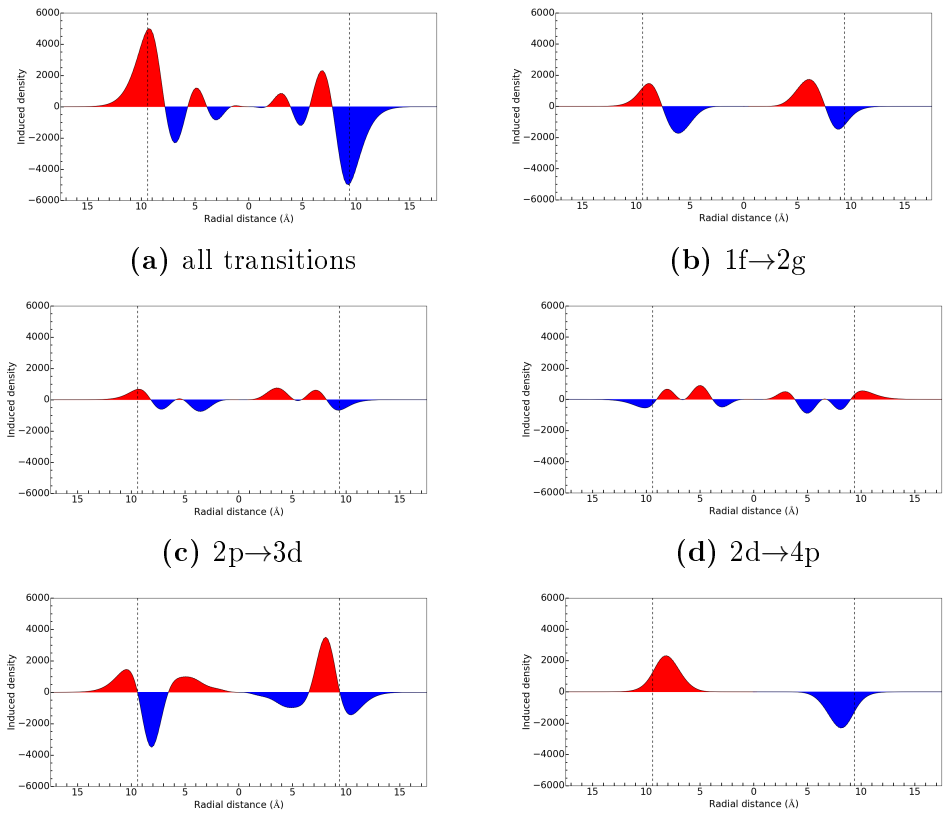

(a) all transitions **(b)** 1f→2g

(c) 2p→3d **(d)** 2d→4p

(e) 1h→3g **(f)** 1h→1i

Figure 15: Radial plots of the induced densities from figure 14. The dashed vertical lines indicate the edges of the jellium sphere.

3.1.4 Spherical cluster Na_{138}

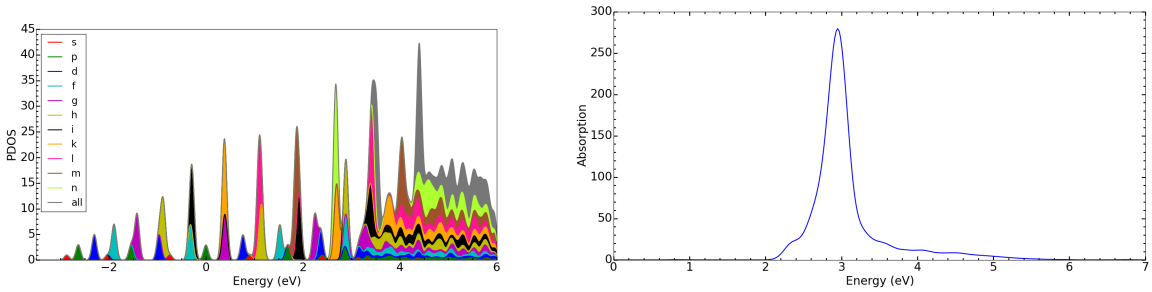

(a) PDOS **(b)** spectrum

Figure 16: The projected density of states and the optical absorption spectrum for the Na_{138} jellium cluster. The HOMO level is set to zero in figure 16a. The width of the Gaussian broadening used for the states in figure 16a was 0.05 eV and the width oif the Gaussian used for the spectrum in figure 16a was 0.1 eV.

The radius of the cluster with 138 electrons was approximately 10.75 Å, and the side length of the unit cell was 38 Å. The projected density of states and the optical absorption spectrum are displayed in figure 16. The HOMO-LUMO gap is not as big as in the clusters with 58 and 92 electrons, but larger than in the cluster with 40 electrons. The HOMO state is the 3p state and the LUMO state the 1k state.

The cut-off energy in the calculation of the optical properties was 6 eV for the Na_{138} jellium cluster. There were 908 states included in the calculations. The spectrum has again only one large peak, as in the spectrum of the Na_{92} jellium cluster. There is also a small peak at about 0.8 eV, not visible in the scale of figure 16b. The large peak is located at 2.95 eV in energy.

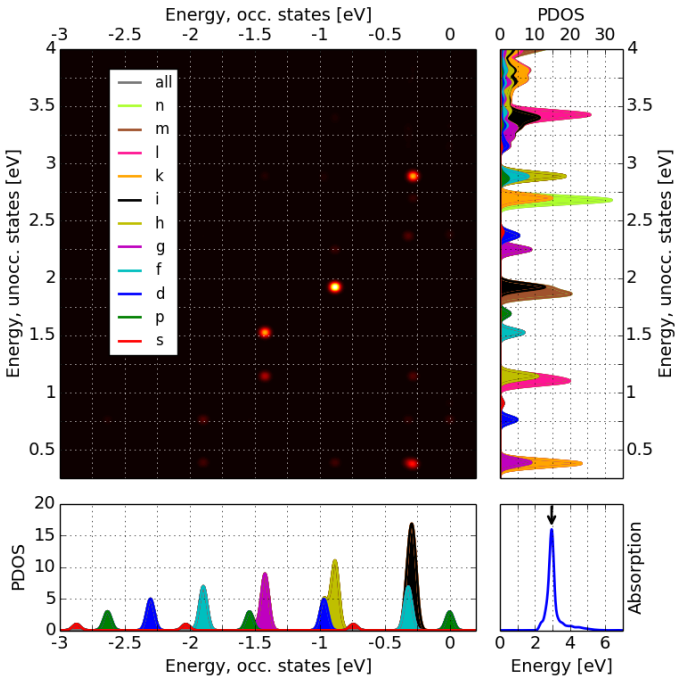

Figure 17: The TCM figure for the large absorption peak for the Na_{138} jellium cluster. See details in the caption of figure 2.

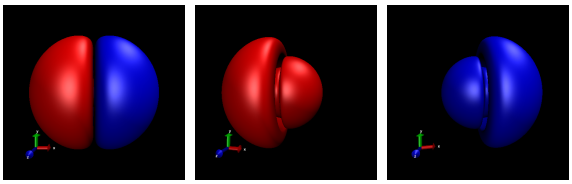

(a) pos. and neg. parts **(b)** positive part **(c)** negative part

Figure 18: Induced density for the largest peak of the Na_{138} jellium cluster. All the figures are in the same length scale. See the caption of figure 3 for details.

The TCM for this large peak can be seen in figure 17. Most of the contributions are again located almost diagonally. The strongest contribution comes from transition 1h→2i. Other transitions with strong contributions are 1g→2h, 1g→3f, 1i→1k (also 2f→2g), and 1i→3h. Other, weaker contributions come for example from the transitions 1f→2g, 1f→3d, 1h→2g, 1h→3g, 2f→3d, 2f→4d, 1i→2h, 1i→2k, 3p→3d, and 3p→4d.

The isosurface of the induced density for the largest peak can be seen in figure 18. The induced density plotted radially is displayed in figure 19. The structure of the induced density is quite similar to the induced densities of the largest peak of the smaller clusters. However, there are more inner shells here than in the induced density of the other clusters.

The five strongest contributions were further analysed. These contributions have been marked with white circles in figure 20. The induced densities caused be these transitions can be seen in figure 22. The number and size of the isosurface shells vary for the different contributions. For the transition 1g→3f, the negative and positive outermost shells are on different sides of the cluster than for the other transitions.

The induced densities from 22 are plotted radially in figure 22. The transitions 1g→2h and 1h→2i both induce similar induced density: a shell of positive and negative density on both sides of the cluster, and all the induced density concentrated near the surface. Transitions 1g→3f and 1i→3h also have similar structures to each other, but the negative and positive areas are reversed. The induced density for the transition 1i→1k looks a little different from the others, possibly because another transition, 2f→2g, also shows up in the same contribution.

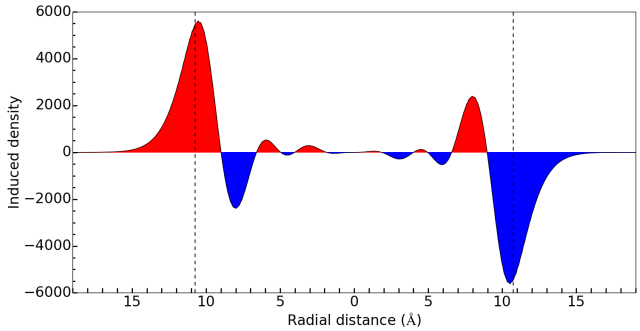

Figure 19: The induced density from figure 18 plotted radially. The dashed vertical lines indicate the jellium edges of the cluster.

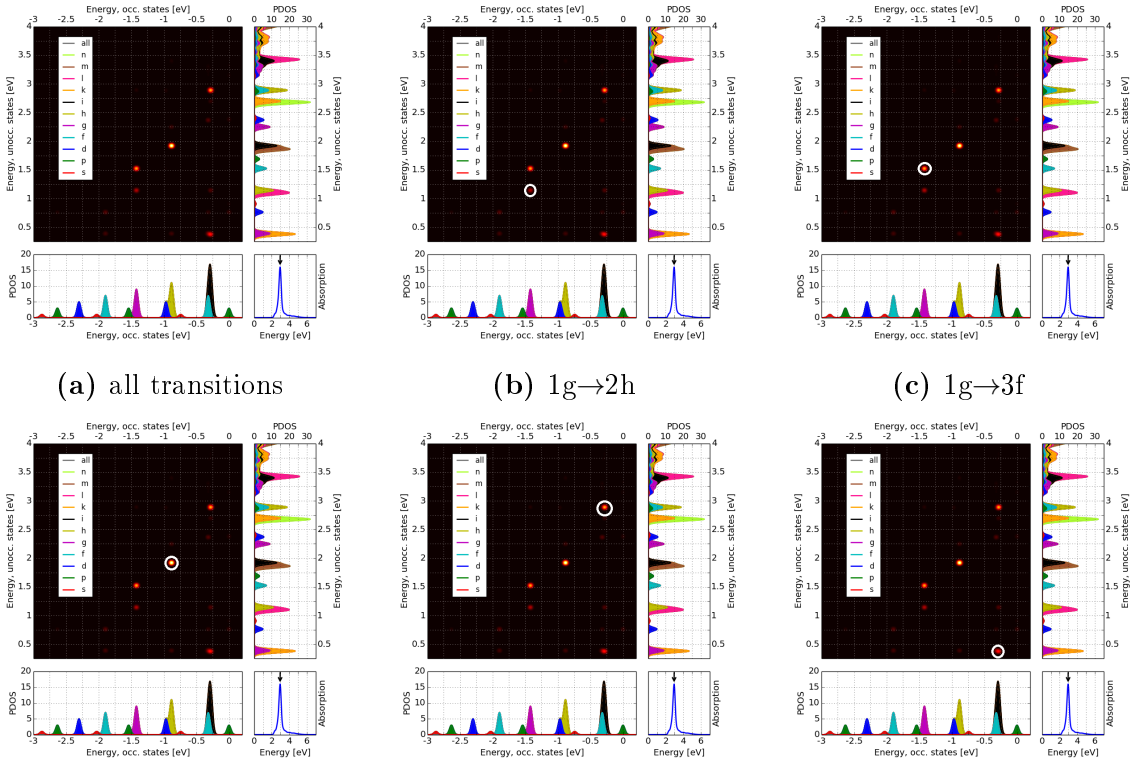

(a) all transitions **(b)** 1g→2h **(c)** 1g→3f

(d) 1h→2i **(e)** 1i→3h **(f)** 1i→1k

Figure 20: The analysed contributions marked with white circles.

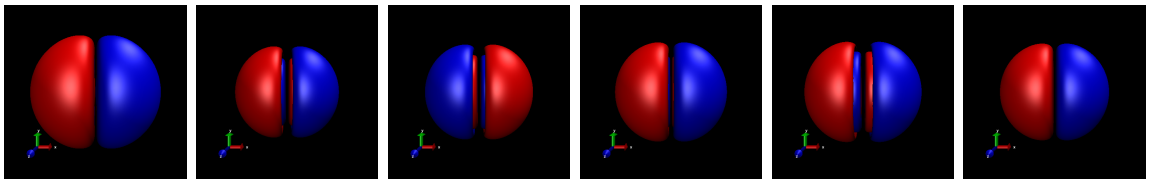

(a) all transitions **(b)** 1g→2h **(c)** 1g→3f **(d)** 1h→2i **(e)** 1i→3h **(f)** 1i→1k

Figure 21: The induced densities for the different transitions. In figure 20a is displayed the induced density for all the transitions contributing to the largest peak. In figures 20b – 20f are the induced densities for the transitions shown in figure 20. All the figures are in the same length scale. See the caption for figure 3 for details.

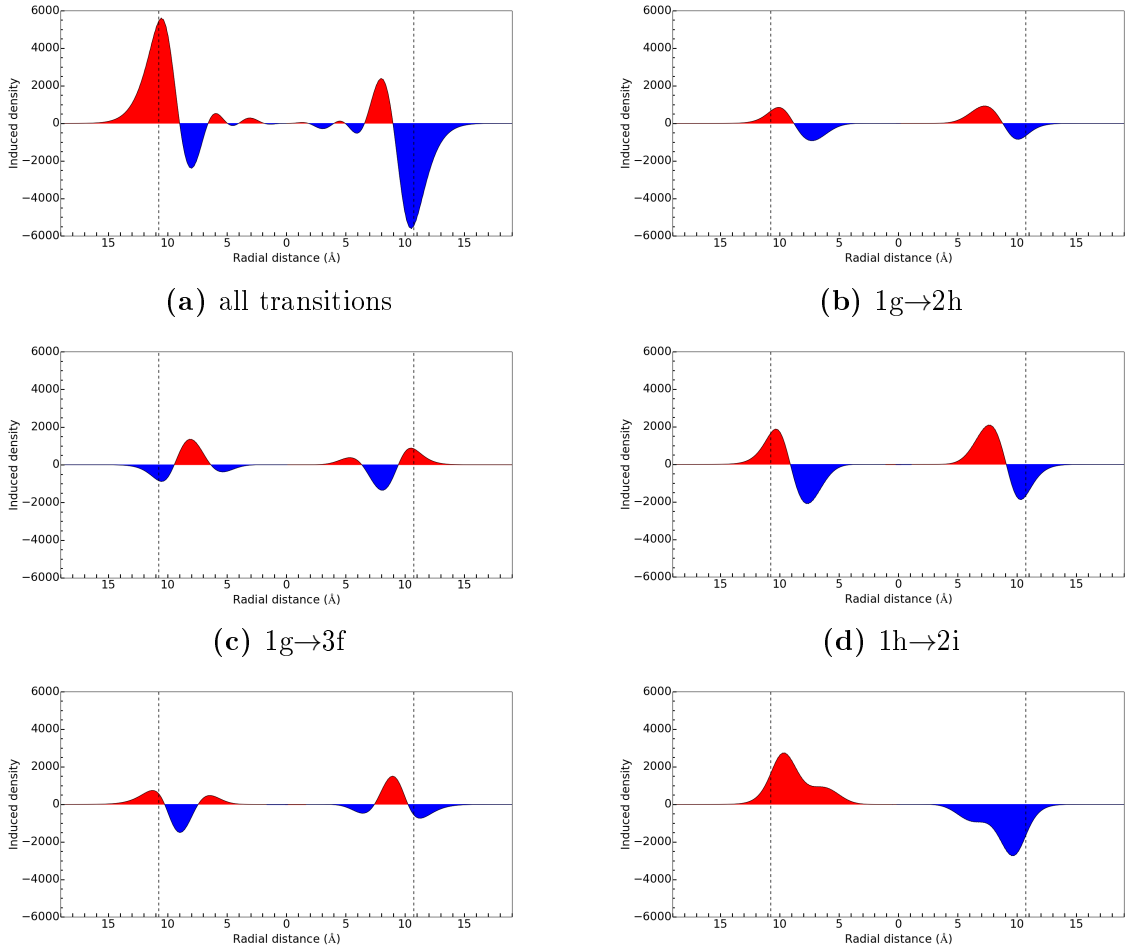

(a) all transitions

(b) 1g→2h

(c) 1g→3f

(d) 1h→2i

(e) 1i→3h

(f) 1i→1k

Figure 22: The induced densities from figure 22 plotted radially along the x axis. The dashed vertical lines indicate the edges of the jellium sphere.

3.1.5 Evolution of the largest absorption peak

The optical absorption spectra of the spherical jellium clusters with 40, 58, 92, and 138 electrons can all be seen in the same scale in figure 23. The change from two peaks via one large peak with a shoulder to a single large peak can be seen clearly. Also, the absorption strength gets larger when the size of the cluster increases. The largest peak is at 2.92 eV for the 92-electron cluster and at 2.95 eV for the 138-electron cluster. Using the free-electron model of electron gas, the energy E_P of the bulk plasmon in sodium can be calculated from

$$E_P = \hbar\omega_P = \hbar \times \sqrt{\frac{ne^2}{\varepsilon_0 m_e}}, \tag{1}$$

where n is the electron density of sodium, e is the elementary charge, ε_0 the permittivity of free space and m_e is the mass of the electron. ω_P is the resonance frequency.

The bulk density can be obtained from the Wigner-Seitz radius of sodium, r_{WS}:

$$n = \left(4/3\pi r_{WS}^3\right)^{-1}. \tag{2}$$

With the Wigner-Seitz radius used here, 2.08 Å, this yields an electron density of approximately 0.0265Å^{-3}. The surface plasmon resonance energy for bulk sodium in the shape of a sphere would then be

$$E_{SP} = \frac{E_P}{\sqrt{3}}. \tag{3}$$

This gives 3.49 eV for surface plasmon resonance for a bulk-sized sodium sphere. Thus, the energies of the surface plasmon peaks here are still about 0.5 eV away from the bulk value, but approaching it slowly.

The TCM plots of the largest peak of each studied cluster are displayed in figure 24. In all these clusters there is clearly a collective transition causing the largest peak, and it gets more collective towards the larger clusters. Also, in the clusters with 58, 92, and 138 electrons, the diagonal band of transitions can be seen, i.e. most of the individual transitions have approximately the same energy.

In terms of there being one large absorption peak caused by many simultaneous transitions, most of them happening at approximately the same energy, it would seem that at least the jellium clusters Na_{58}, Na_{92} and Na_{138} have a SPR peak. Cluster Na_{40} has two large absorption peaks caused by collective transitions, and these peaks could be seen as a split SPR peak.

The induced densities plotted radially for the studied clusters can be seen in figure 25. The main structure of the induced density for the largest peak is very similar for all the clusters studied. The largest oscillations of electron density happen near the surface, but there are also smaller oscillations inside the sphere, some of them in the opposite direction. As the cluster gets larger, the peak value of the induced density also gets larger, and a bigger percentage of the induced density is concentrated near the surface of the sphere.

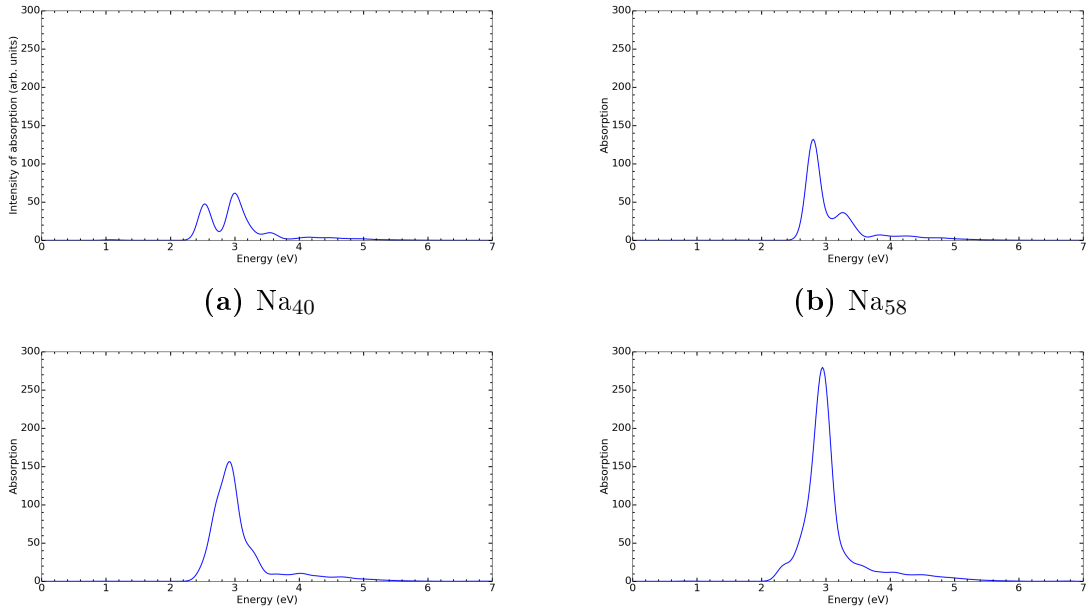

(a) Na_{40} **(b)** Na_{58}

(c) Na_{92} **(d)** Na_{138}

Figure 23: The optical absorption spectra for the spherical jellium clusters with the density of sodium and with 40, 58, 92, and 138 electrons.

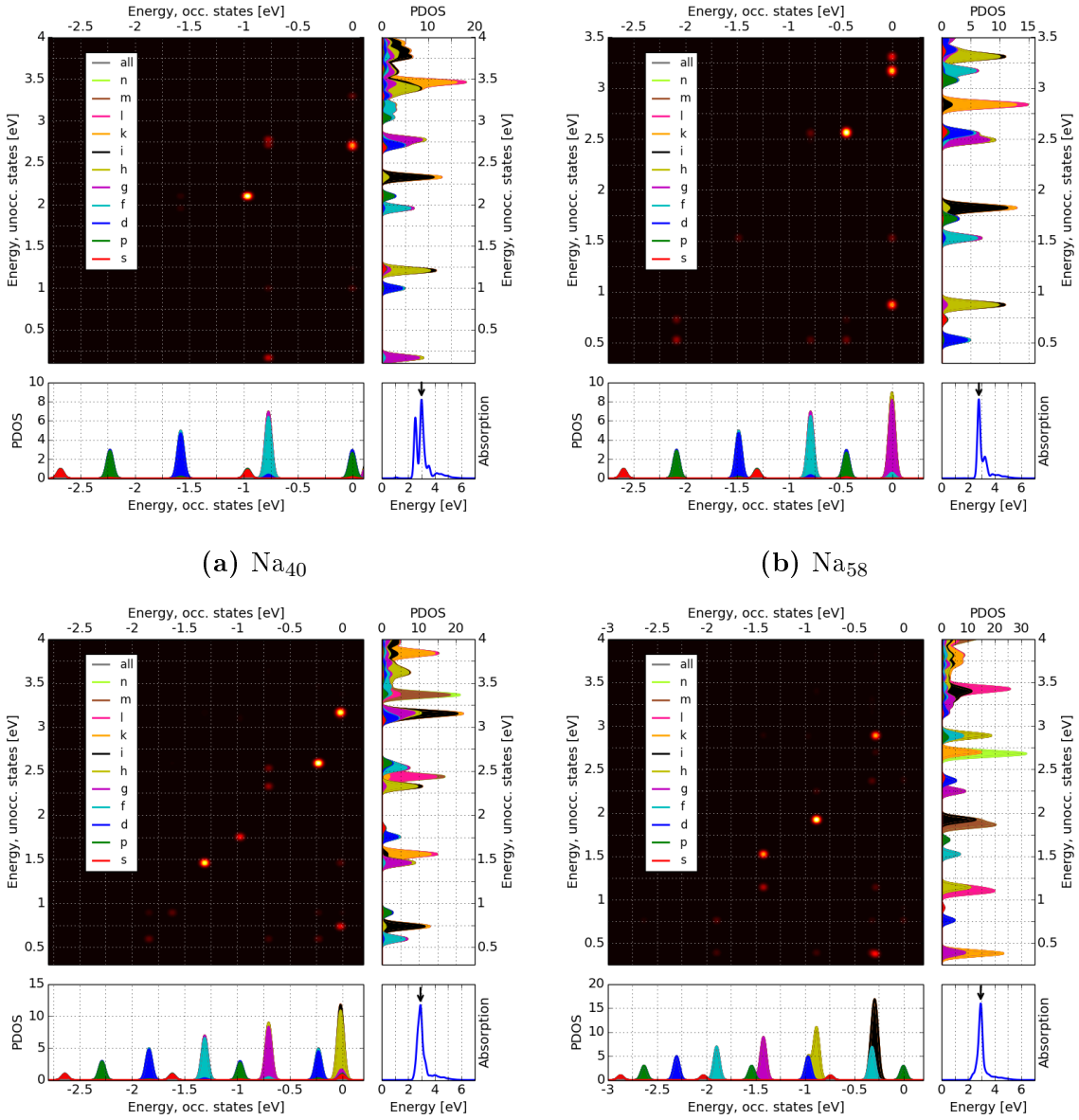

(a) Na_{40} **(b)** Na_{58}

(c) Na_{92} **(d)** Na_{138}

Figure 24: TCM plots for the spherical jellium clusters with the density of sodium and with 40, 58, 92, and 138 electrons. The dashed vertical lines indicate the edges of the jellium spheres.

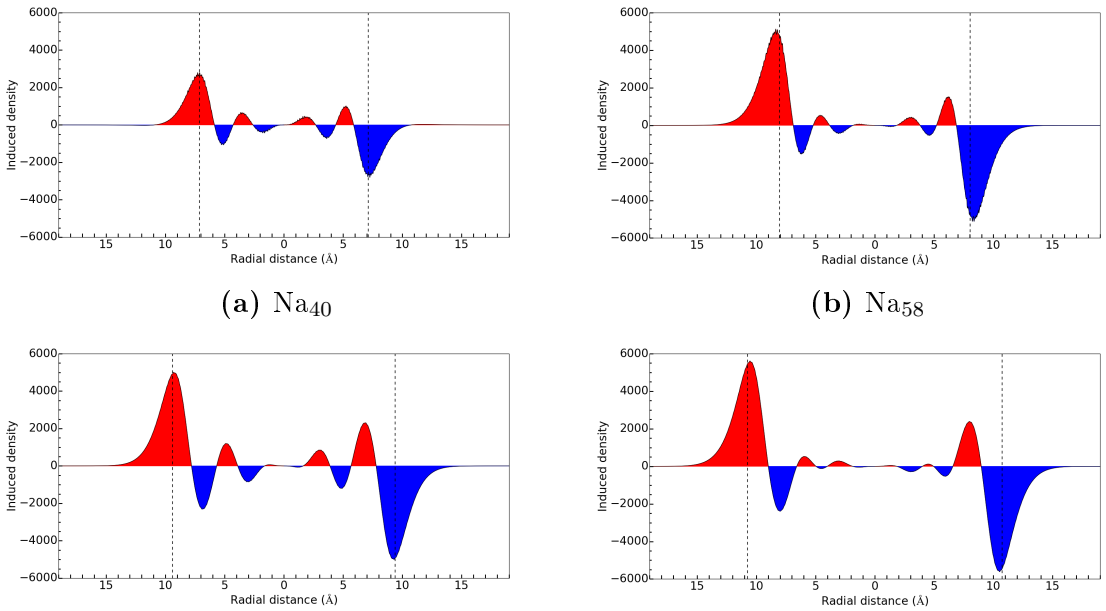

(a) Na_{40} **(b)** Na_{58}

(c) Na_{92} **(d)** Na_{138}

Figure 25: Indced densities plotted radially for the spherical jellium clusters with the density of sodium and with 40, 58, 92, and 138 electrons.

3.1.6 Comparison with other jellium studies

Guet and Johnson studied the optical properties of small jellium clusters using the Hartree-Fock approximation for the ground state calculation and RPA for the dipole excitation spectra [28]. A Wigner-Seitz radius of 4 $a_0 \approx 2.12$ Å was used. The dipole oscillation strengths from this study for the jellium clusters Na_{40} and Na_{92} can be seen in figure 26.

Yannouleas et al. also used RPA to calculate the optical spectra of small jellium clusters [29]. The Wigner-Seitz radius used in this study was also 4 a_0. The RPA cross-sections for the jellium clusters Na_{40}, Na_{58}, Na_{92}, and Na_{138} are displayed in figure 27.

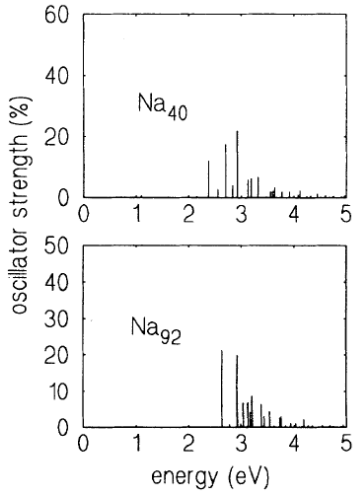

Figure 26: The oscillator strengths for jellium clusters with the density of sodium and 40 and 92 electrons. The oscillator strengths are given as percentage of the Thomas-Reiche-Kuhn f sum rule. The figure is part of a figure from reference [28].

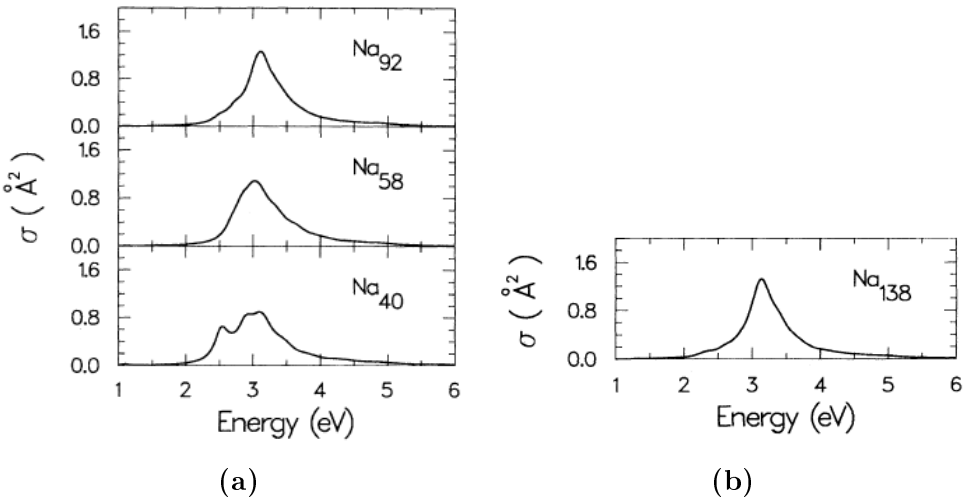

(a) (b)

Figure 27: RPA oscillator strengths folded by a Lorentzian for the jellium clusters Na_{40}, Na_{58}, Na_{92}, and Na_{138}. An intrinsic width of 10% was used for the Lorentzian. The figures 27a and 27b are parts of figures from reference [29].

Comparing figures 26 and 27 to figure 23, the overall shapes of the spectra calculated with GPAW seem to match those obtained in previous studies. In the spectrum of Guet and Johnson, the spectra of Na_{40} has three larger peaks. In the spectrum of Yannouleas et al., there are two larger peaks, but the larger is slightly split. In both spectra, the first large peak is smaller than the ones after it. This matches the two-peaked spectrum made with GPAW. Also, the positions of the peaks are very similar in the spectrum of this study and the spectrum of Yannouleas et al. The first large peak of Guet and Johnson is also at approximately the same energy as this peak in the other two spectra.

The spectrum of Na_{58} in figure 27a has a larger tail on the right than the spectrum made with GPAW in figure 23b. However, the spectrum of Yannouleas et al. does not have as clear a second peak as the GPAW spectrum, and the peak of Yannouleas et al. is a little higher energy. The overall shapes are still similar.

The spectrum of Na_{92} is very similar in all three cases. The largest peak is at about the same energy in the spectrum of Guet and Johnson and the GPAW spectrum of this study. The peak of the spectrum of Yannouleas et al. is a little higher in energy, but the crooked shape is very similar to that of the spectrum of this study.

The spectrum of Na_{138} obtained in this study is quite similar to the one in the study of Yannouleas et al., although the peak is narrower in the spectrum calculated with GPAW. Also the peak of Yannouleas et al. is again a little higher in energy.

To summarize, the main features of the spectra made with GPAW are similar to the those of the spectra of the earlier studies. Also the energies of the peaks are approximately the same. The small difference in the jellium density and differences in the calculation method for the optical spectra may explain why the energies of the peaks differ slightly.

3.2 A cuboctahedral cluster with 138 electrons

The cluster in the shape of a regular cuboctahedron had 138 electrons, and the side length of its faces was approximately 13.0 Å. The side length of the unit cell was 42 Å. The positive jellium density of the cluster and the electron density of the ground state can be seen in figure 28.

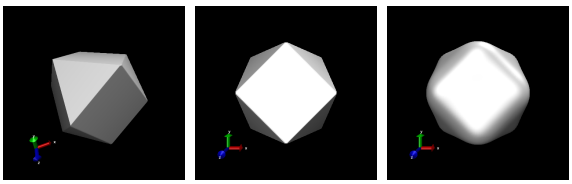

(a) jellium background density

(b) jellium background density

(c) electron density

Figure 28: In figures 28a and 28a is displayed the positive jellium background density of the jellium Na_{138} cuboctahedron from two different directions. In figure 28c is displayed an isosurface of the electron density of the cluster viewed from the same direction as figure 28b. The isosurface value is the density of the jellium background.

The projected densities of states of the Na_{138} jellium cuboctahedron and sphere can be seen in figure 29. The change from a sphere to a cuboctahedron has caused a considerable amount of splitting in the electronic states. The HOMO-LUMO gap is also very small, and the density of states is almost continuous after the HOMO state for the cuboctahedron.

The optical spectra of the two Na_{138} jellium clusters of different shapes can be seen in figure 30. The energy cut-off was 6 eV for both these clusters, and for the sphere this meant that the 908 lowest states and for the cuboctahedron the 1183 lowest states were included in the calculation. There is only one peak in both spectra, but the peak of the cuboctahedron is clearly smaller, a little narrower, and positioned a little lower in energy than the peak of the sphere: the peak of the sphere is at 2.95 eV, the peak of the cuboctahedron at 2.83 eV. The change in shape can therefore be clearly seen in the optical absorption spectrum.

The TCM figures for the two studied clusters with 138 electrons are shown in figure 31. Similar transitions can be seen in both figures, but because the Kohn-Sham states are split and as a results the density of states is almost constant for the cuboctahedron, there

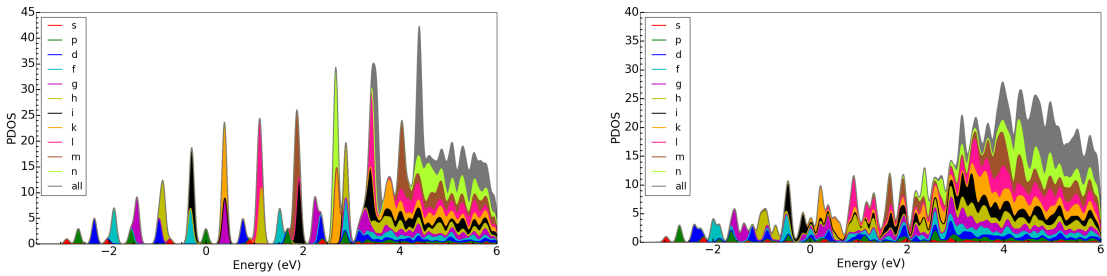

(a) sphere

(b) cuboctahedron

Figure 29: The projected densities of states for the Na_{138} jellium sphere and cuboctahedron. The width of the Gaussian broadening used for the states was 0.05 eV in both figures. The HOMO levels have been set to zero.

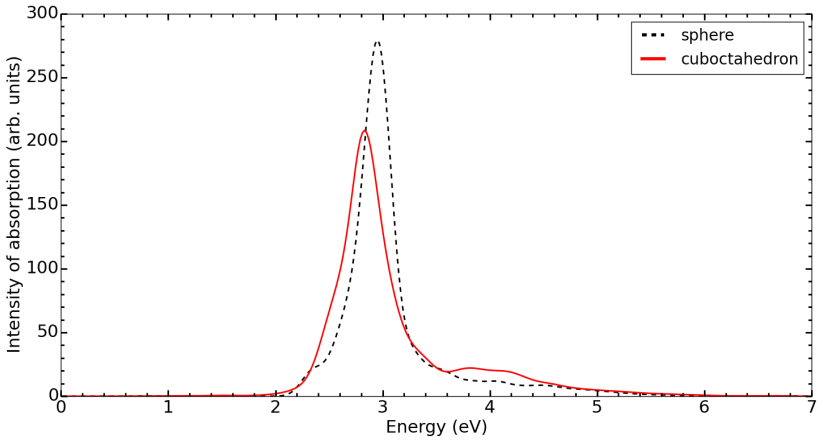

Figure 30: The optical absorption spectra for the Na_{138} jellium sphere and cuboctahedron plotted in the same figure. The width of the Gaussian broadening used was 0.1 eV.

are many more transitions in the TCM plot of the cuboctahedron than in the TCM plot of the sphere. For the cuboctahedron the diagonal belt of transitions is very prominent. The TCM analysis thus shows a distinct difference between the two clusters of different shapes.

The induced densities for the two clusters are displayed in figure 32. The white dots show the edges of the positive jellium background charge of the clusters. As can be seen, the oscillation of the charge density follows the shape of the cluster. The shape of the induced density is more complex in the case of the cuboctahedron, but the main structure of inner shells of opposite densities is the same for both clusters. This can be seen better in figure 33, where the induced densities are plotted radially: the peak values of the densities are larger for the sphere, but the main structure is very similar in both clusters. The clearest difference is that in the case of the cuboctahedron the largest and outermost shell of

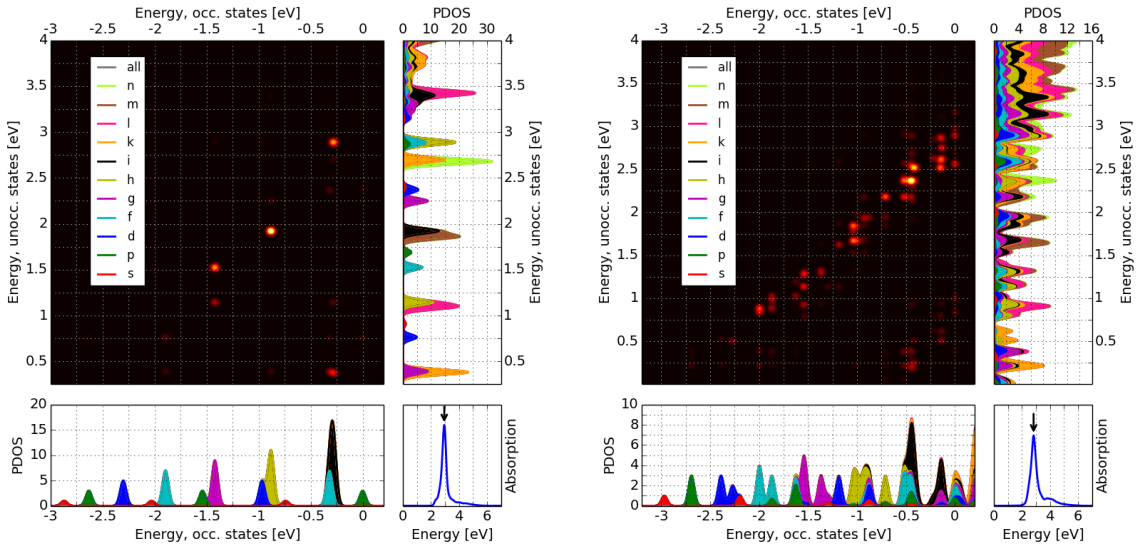

(a) sphere **(b)** cuboctahedron

Figure 31: The TCM figures for the largest peak for the Na_{138} cuboctahedron and sphere jellium clusters. For details see the caption of figure 2.

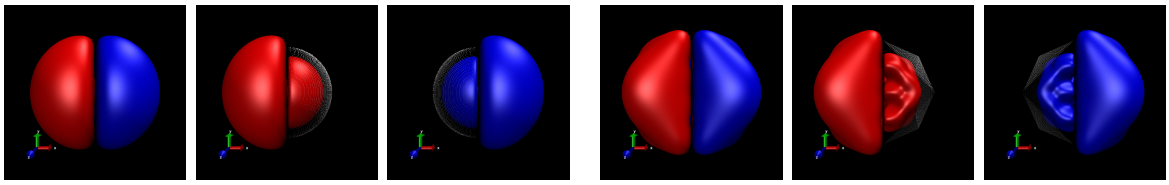

(a) sphere **(b)** sphere, positive part **(c)** sphere, negative part **(d)** cuboctahedron **(e)** cuboctahedron, positive part **(f)** cuboctahedron, negative part

Figure 32: Induced densities for the largest peak for the Na_{138} cuboctahedron and sphere jellium clusters. The red and blue colours represent isosurfaces with the value of the jellium density and its negative, respectively. The white points mark the edges of the positive jellium background densities. Note that the figures for the sphere and the cuboctahedron are not in the same length scale. The images have been made with VMD.

induced density is outside the positive jellium background charge, whilst it is located on the surface in the case of the jellium sphere.

To sum up, the main features of the optical spectra, TCM figure, and induced density remain the same when the shape of the 138-electron cluster is changed from a sphere to a cuboctahedron, but the change in shape can still be observed clearly in the details of these optical properties.

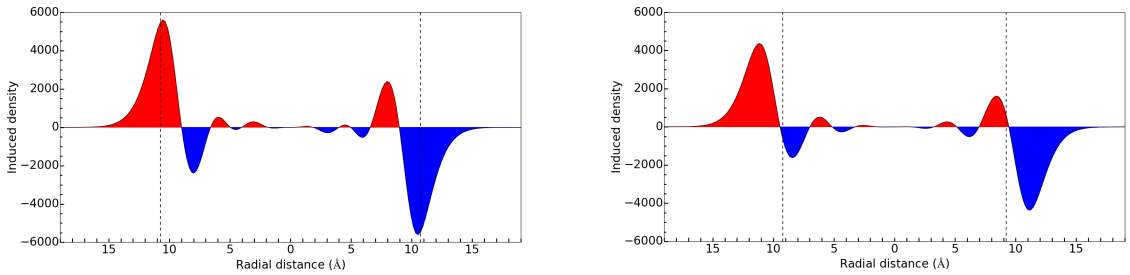

(a) sphere **(b)** cuboctahedron

Figure 33: The induced densities from figure 32 plotted radially along the x axis. The dashed vertical lines show the edges of the clusters.

3.3 Two spherical clusters with 8 atoms

Six systems with two spherical Na_8 jellium clusters, i.e. a Na_8 dimer, were studied. The two clusters were placed near one another, with the separation varying from half the

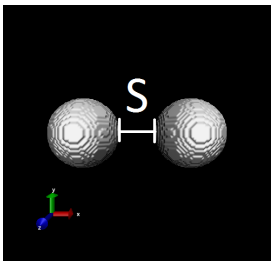

Figure 34: One system with two adjacent jellium spheres. In this case the separation S between the spheres is equal to the radius r of the spheres. The two spheres are identical in shape, size, and charge.

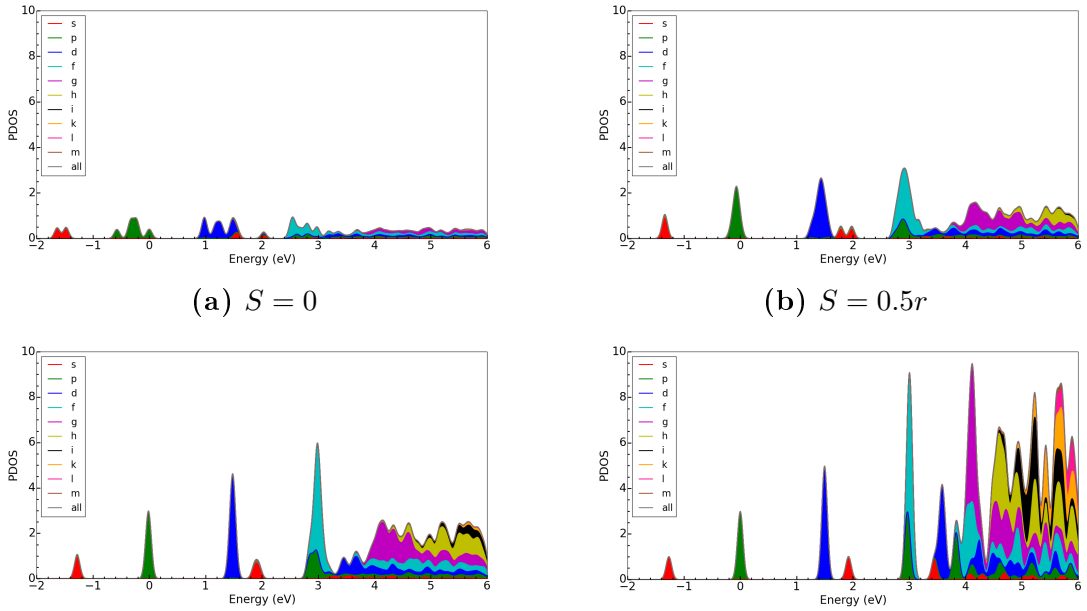

(a) $S = 0$ **(b)** $S = 0.5r$

(c) $S = r$ **(d)** single sphere

Figure 35: The projected density of states for the systems of two Na_8 jellium spheres with separations $S = 0$, $S = 0.5r$, and $S = r$. The figure in the bottom right corner is the PDOS of a single sphere, included for comparison. The HOMO level has been set to zero in all the figures. A Gaussian distribution with a width of 0.05 eV was used in the broadening of the states.

length of the radius to four times the length of the radius. The radius of the spheres, r, was 4.16 Å. A case were the spheres were touching each other (i.e. separation of 0 Å) was also studied. The separation S was the distance between the jellium edges of the two clusters. One such system, with $S = r$, can be seen in figure 34. The optical spectrum was calculated for each system. A TCM analysis was also performed for the largest peak and for smaller peaks lower at energy, and the induced densities were plotted for these peaks. For the system with $S = r$, the induced densities for the strongest contributions for the largest peak were also separately studied. The evolution of these optical properties with growing separation was studied, and the results were compared to those of a single 8-electron sphere.

In figure 35 are shown the PDOS figures for one of the spheres of the systems with separations 0, $0.5r$, and r. The PDOSs of the two spheres in the same system are identical. The PDOS figure of a single sphere is also shown for comparison. The projected densities of states for the systems with $S = 1.5r$, $S = 2r$, $S = 3r$, and $S = 4r$ are shown in figure 36. Note that for the system with $S = 4r$ the states have been plotted only up to 5 eV, because for this cluster the Kohn-Sham electron states were not converged up to 6 eV from the HOMO level, and the maximum energy difference in the lr-TDDFT calculations was 5eV.

The PDOS calculations were limited inside a sphere with the centre in the centre of one of the jellium clusters. The radius of this sphere was chosen for each system so that the sphere was as large as possible without including parts of the other cluster and while staying inside the calculation box. This was done so that the states of one cluster would not be included in the PDOS figure of the other cluster. Because of this, the states of higher angular momentum (after f) are not featured very prominently in the PDOS figures

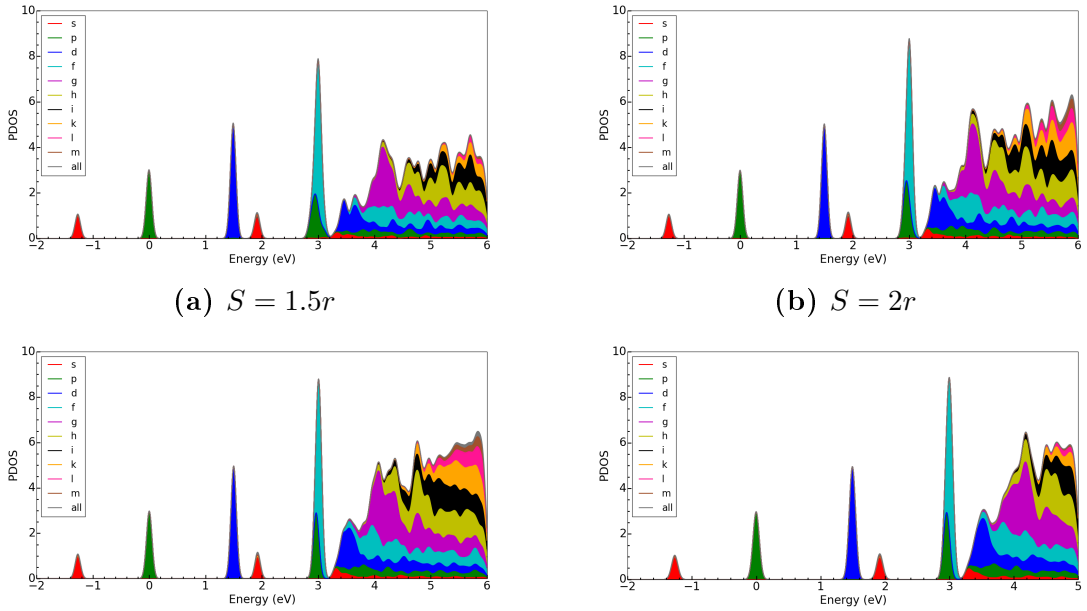

(a) $S = 1.5r$ **(b)** $S = 2r$

(c) $S = 3r$ **(d)** $S = 4r$

Figure 36: The projected density of states for the systems of two Na_8 jellium spheres with separations $S = r$, $S = 1.5r$, $S = 2r$, $S = 3r$, and $S = 4r$. Note that for the system with $S = 4r$ in figure 36d the states are only plotted up to 5 eV in energy. The HOMO level has been set to zero in all the figures. A Gaussian distribution with a width of 0.05 eV was used in the broadening of the states.

of the systems with small separations.

As can be seen from figure 36, when $S = 1.5r$, the six lowest electron states are already almost identical to the states of an isolated sphere. With smaller separations, there is some splitting in the states. In the case of the system with $S = r$, there is visible splitting only in 2p and 1f states. A very clear HOMO-LUMO gap can be seen in all the systems in figures 35 and 36, although, because of splitting of the states, it is slightly smaller in the systems with $S = 0$ and $S = 0.5r$.

In figure 37 can be seen the optical absorption spectra of the systems with $S = 0$, $S = 0.5r$, and $S = r$. The optical spectra of a single sphere is also included for comparison. In figure 38 are the spectra for systems with $S = 1.5r$, $S = 2r$, $S = 3r$, and $S = 4r$. The cut-off energy in the lr-TDDFT calculation was 6 eV for the systems with a separation of $3r$ or smaller, and 5 eV for the system with $S = 4r$. The lowest 411, 427, 598, 596, 673, and 629 Kohn-Sham states were included in the calculation for the systems with $S = 0$, $S = 0.5r$, $S = r$, $S = 1.5r$, $S = 2r$, $S = 3r$, and $S = 4r$, respectively. For the single sphere, the energy cut-off was 7 eV, and the 232 lowest states were included in the calculation.

Already when the separation S is the length of the radius, in this case 4.16 Å, the spectrum is very close to the spectrum of a single sphere. The spectra of the systems with separations of $1.5\,r$ or more are almost the same shape as the spectrum of the single sphere. Of the systems in figures 37 and 38, only the ones with separations of $S = 0$ and $S = 0.5r = 2.08$ Å, differ clearly from the system of only one sphere optically. The system with $S = 0$ has two and the systems with $S = 0.5r$ three absorption peaks before the largest peak. The system with zero separation is actually a single cluster with a peanut shape, and its energy levels differ quite a lot from those of a single sphere, as can be seen from figure 35 The spectrum of the system with $S = 0.5r$ is a intermediate between the spectra of

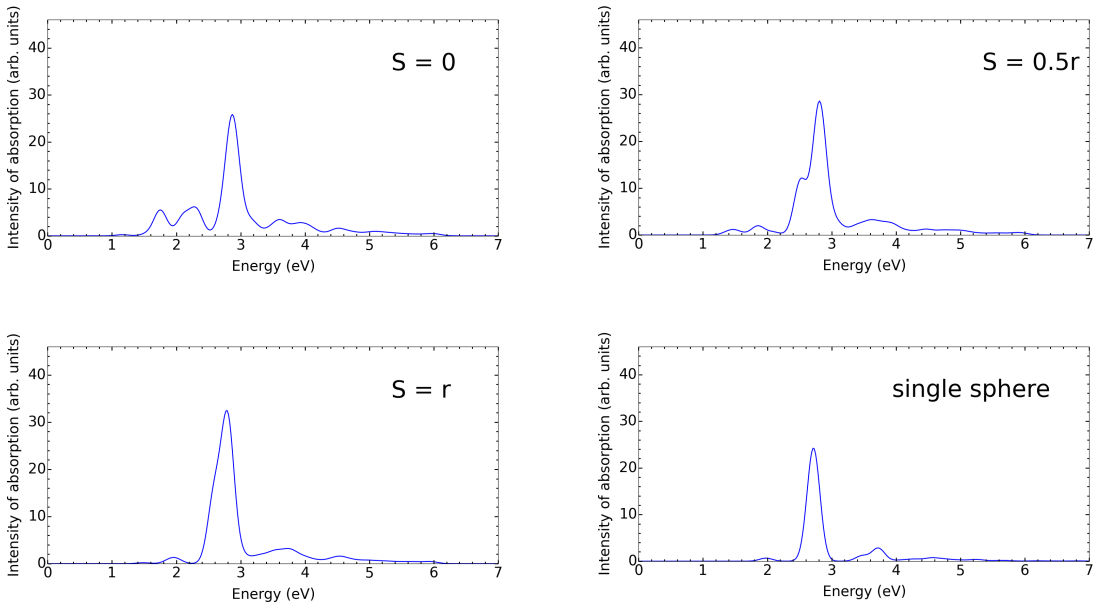

Figure 37: The optical absorption spectra for the systems of two Na_8 jellium spheres with separations $S = 0$, $S = 0.5r$, and $S = r$. The optical spectrum for a single sphere is also included. The cut-off energy was 7 eV for the single sphere and 6 eV for the other systems.

the $S = 0$ system and the $S = r$ system. At least in the case of two Na_8 jellium spheres, the two adjacent clusters have to be very close to each other, if the shape of the optical spectrum is to differ significantly from the spectrum of a single cluster.

The intensity of the maximum absorption is larger in the case of two clusters than in the case of a single cluster, and it gets bigger when the separation between the clusters gets

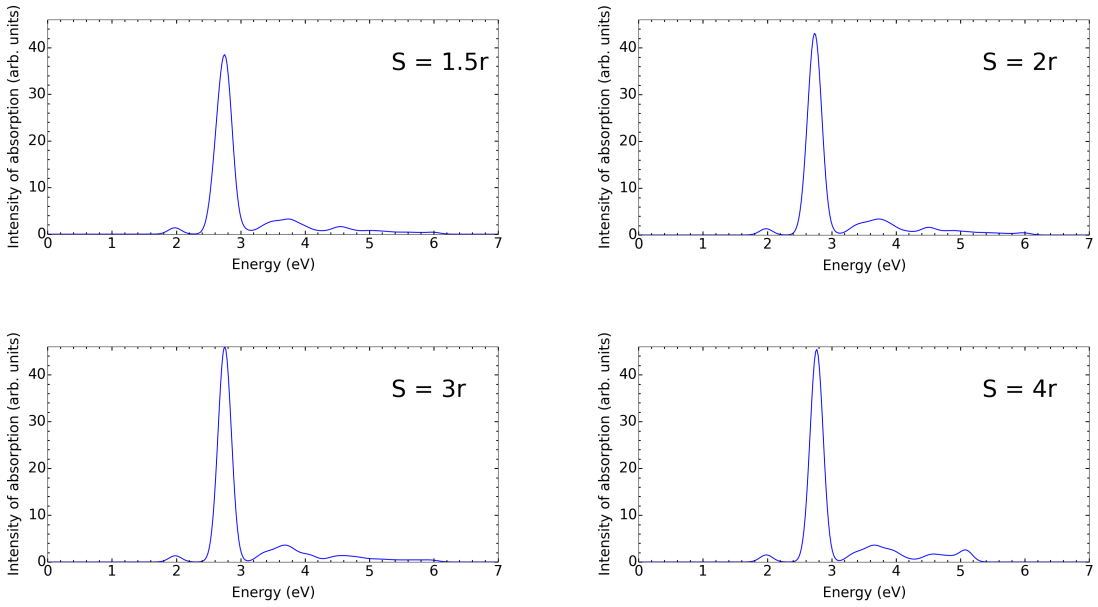

Figure 38: The optical absorption spectra for the systems of two Na_8 jellium spheres with separations $S = 1.5r$, $S = 2r$, $S = 3r$, and $S = 4r$. The cut-off energy was 5 eV for the system with $S = 4r$ and 6 eV for the other systems.

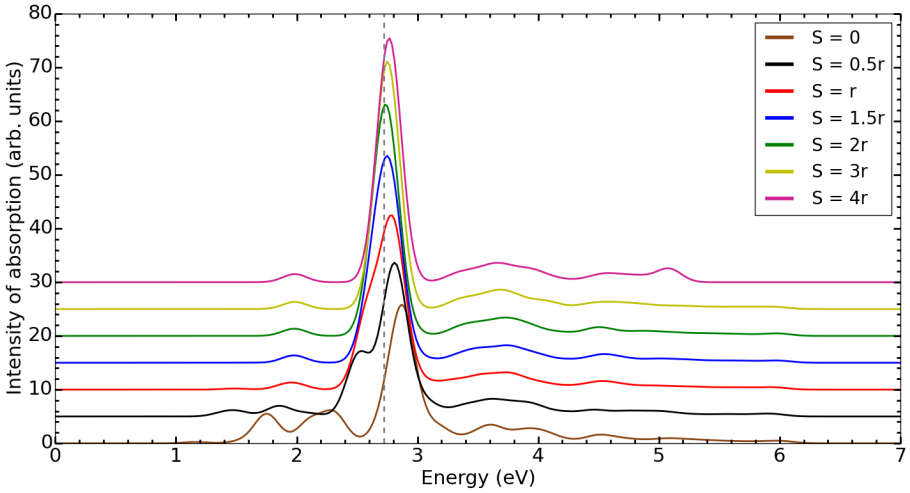

Figure 39: Waterfall plot of the spectra for the systems with two adjacent spheres. The dashed vertical line shows the energy of the peak in the spectrum of a single sphere.

larger. The peak for the system with $S = 4r$ is of smaller intensity than the peak for $S = 3r$, but that is probably due to the smaller cut-off energy in the optical spectrum calculation for the $S = 4r$ system. The 5 eV cut-off energy also presumably causes the small bump just after 5 eV in the optical spectrum of the $S = 4r$ system, which is not present in the other spectra.

In figure 39 all the spectra for the the systems of two adjacent clusters are plotted in the same waterfall plot. The zero level of the intensity is raised by five units with respect to the previous system for all systems with a separation more than zero. The dashed vertical line indicates the energy of the absorption peak for a single cluster. The energy of the largest peak changes when the separation between the clusters changes. The small peak at just under 2 eV, which is also present in all the systems, stays at the same energy for the clusters with separation of the length of the radius or larger.

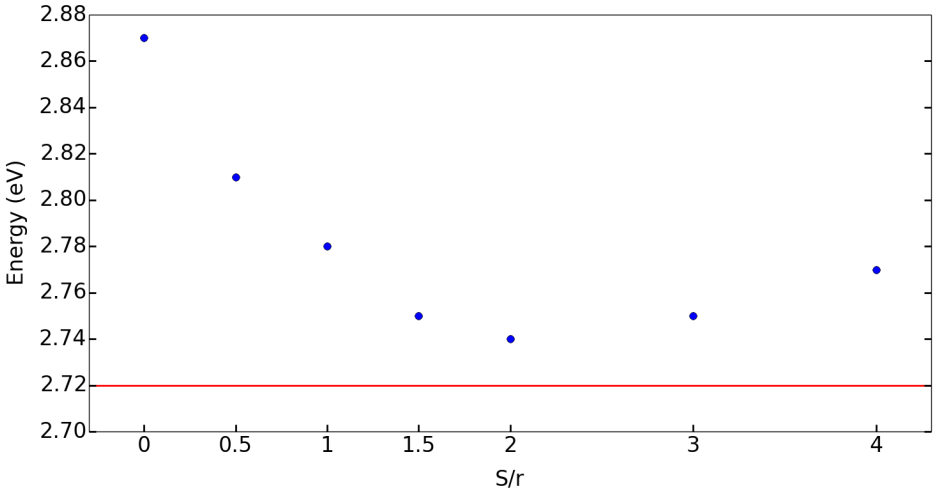

Figure 40: The energy of the largest absorption peak as a function of the separation versus radius ratio, S/r. The red horizontal line indicates the energy of the largest peak for a single, isolated sphere.

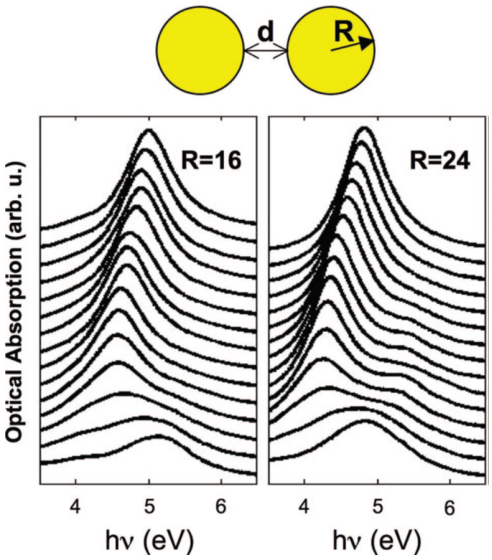

Figure 41: Absorption spectra for the systems with two spheres with the radius $R = 16a_0$ (left) and with radius $R = 24a_0$ (right). The separations (marked d in the figure) are 0, 1, 2, 3, 4, 5, 6, 7, 8, 10, 12, 14, 16, 20, and 24 a_0 from bottom to top. An energy broadening with a width of of 0.27 eV has been used for the spectra. The figure is taken from reference [30].

The energies of the tallest absorption peaks have been plotted against the separation versus radius ratio, S/r, in figure 40. The energy of the absorption peak of a single cluster is indicated by the red horizontal line. As can be seen, the energy of the absorption peak gets smaller as the separation between the two clusters grows for the systems with separation ranging from 0 to $2r$. The shift is not linear: the change in energy gets smaller when the separation gets bigger. After $S = 2r$ the energy starts to get bigger when the separation grows. However, the change in energy between systems with $S = 4r$ and $S = 3r$ is much smaller than the change in energy between systems $S = 2r$ and $S = r$. To summarize, when the separation between the clusters gets smaller, the largest absorption peak first experiences a red shift and then a blue shift in energy. The blue shift seems to be stronger than the red shift.

Zuloaga, Prodan, and Nordlander have investigated the optical spectra of two adjacent spherical jellium particles [30]. They studied two kinds of systems, one with 302 and one with 509 valence electrons in each sphere. The smaller spheres had a radius of 16 $a_0 \approx 8.46$ Å an the larger 24 $a_0 \approx 12.70$ Å. The Wigner-Seitz radius used was 3.0 $a_0 \approx 1.59$ Å, so the charge density was bigger than in this study. The calculations were done using LDA for the ground state calculation and TDLDA and RPA for the optical absorption spectra.

A waterfall plot for the absorption spectra of these systems with different separations can be seen in figure 41. The separations, marked d in the figure, are 0, 1, 2, 3, 4, 5, 6, 7, 8, 10, 12, 14, 16, 20, and 24 a_0 from bottom to top. The trend in this figure is the same as in figure 39: when the separation between the spheres gets smaller, the energy of the largest peak first gets smaller and then starts to get bigger again.

Zuloaga et al. explained the shifts in energy. The blue shift as the separation increases for the systems with large separation is a classical effect caused by the electromagnetic interactions between the two spheres. It can be explained using the classical plasmon hybridization model for dimers [24]. In this region the largest absorption peak is the bonding dipolar plasmon (BDP) peak. For smaller separations the largest absorption

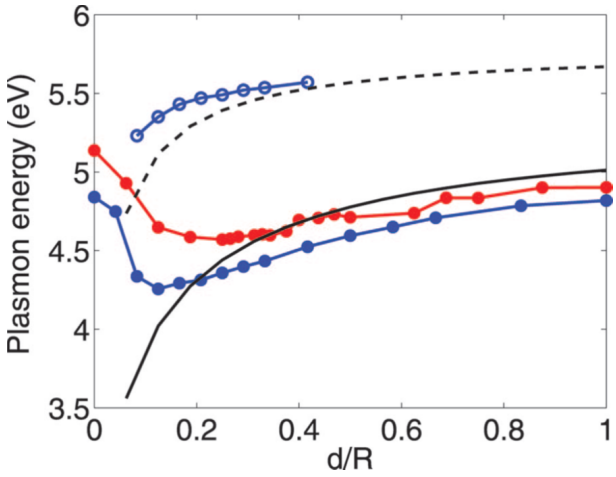

Figure 42: The energies of the absorption peaks from figure 41 as a function of the separation versus radius ratio, d/R in the figure. Red spheres represent the system with the spheres of radius $R = 16a_0$ and the blue spheres the system with $R = 24a_0$. Full spheres are for the largest absorption peak (BDP/CTP) and open spheres for the quadrupole dimer peak. The black lines are the plasmon peak energies calculated using the classical plasmon hybridization model: solid line for the dipolar plasmon peak and dashed for the quadrupolar. The figure is taken from reference [30].

peak is the charge transfer plasmon (CTP), and this peak experiences a red shift when the separation gets bigger. Here, in addition to the two spheres getting polarized individually, there is also a flow of electrons between the clusters. Between the CTP and BDP regions there is a crossover region, where charge is not freely flowing across the junction, but electrons are tunnelling across it. The tunnelling of electrons reduces the electric field and thus the electromagnetic couplings between the spheres. For this reason the blue shift is reduced, and the energy of the peak stays almost constant in this region.

In the case of the system with the larger clusters with a radius of 24 $a_0 \approx 12.70$ Å there is also present a bonding hybridized quadrupole dimer peak for separation of less than 10 a_0. This peak occurs at higher energy than the largest peak.

The energies of the largest peaks and the quadrupole peaks from figure 41 as a function of the separation versus radius ration (d/R in the figure) can be seen in figure 42. The full red spheres represent the largest plasmon peak (CTP/BDP) for the systems with spheres of radius $R = 16a_0$ and the full blue spheres the largest peak for the systems with $R = 24a_0$. Comparing figure 42 to figure 40, the trend can be seen to be the same. However, in the case of the systems in the study of Zuloaga et al., the minimum of energy is reached around 0.2 in terms of separation divided by radius. In this study the minimum is reached somewhere between $S = 2r$ and $S = 3r$. In Angstroms, in the study of Zuloaga et al., the minimum energy is reached at a separation of about 1.5–2 Å for both sizes. In this study, the minimum is reached when the separation is between 8.32 Å and 12.48 Å. This might be due to difference in size (the clusters in the study of Zuloaga et al. had hundreds of electrons, the clusters in this study only eight electrons each) or density (the Wigner-Seitz radius of the clusters in the study of Zuloaga et al. was approximately 1.59 Å, here a Wigner-Seitz radius of 2.08 Å was used).

A TCM analysis was performed for all the systems for the largest peaks and all peaks below it in energy. The TCM figures were compared to each other and the TCM figure of a single Na_8 jellium sphere.

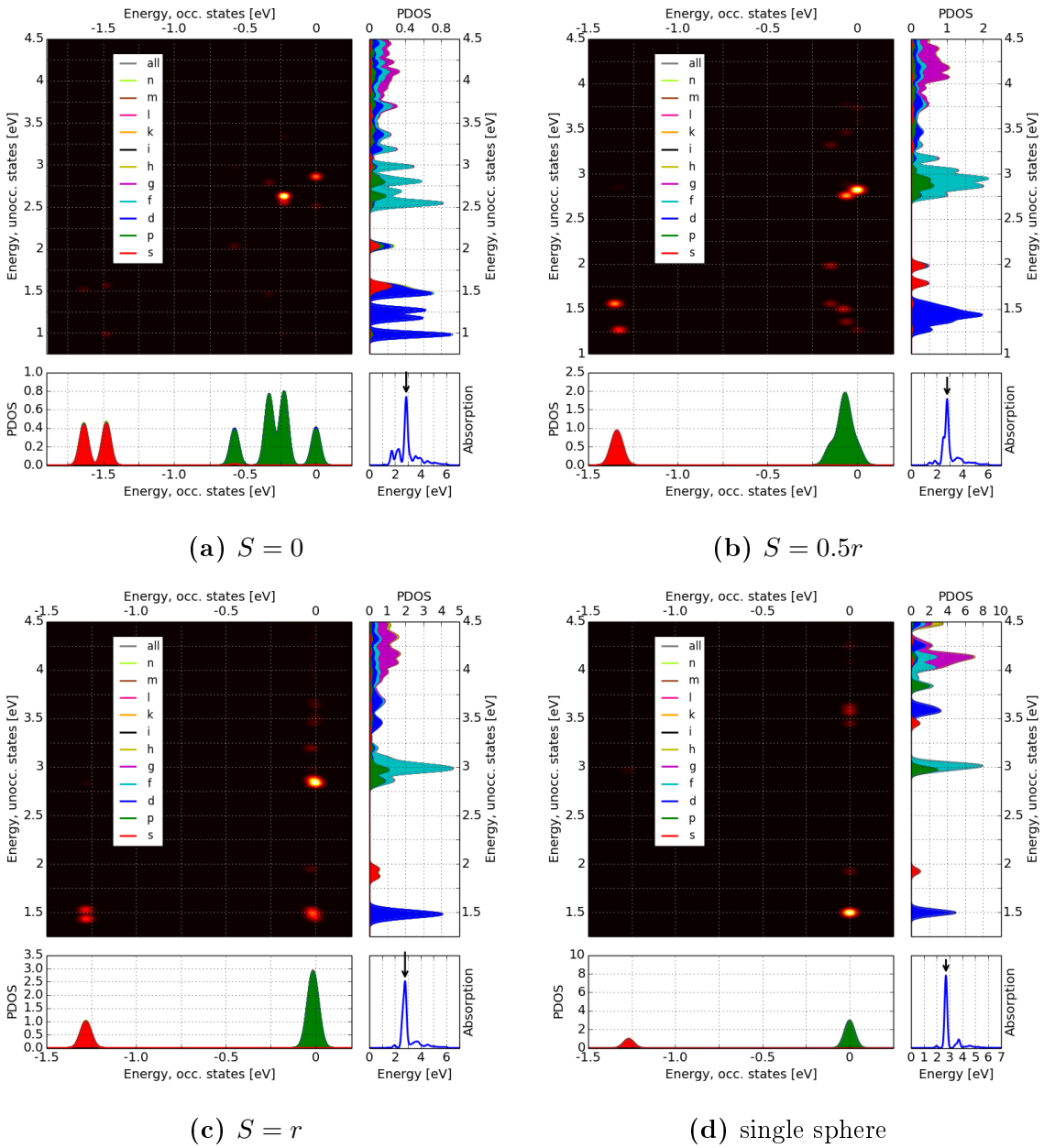

(a) $S = 0$ **(b)** $S = 0.5r$

(c) $S = r$ **(d)** single sphere

Figure 43: TCM plots for the largest peak for the systems of two Na_8 jellium spheres with separations $S = 0$, $S = 0.5r$, and $S = r$. The TCM plot of a single sphere is also included. Note that the energy scales are not necessarily the same in all the figures. For details see the caption of figure 2.

The TCM plots of the largest absorption peak for clusters with separations $S = 0$, $S = 0.5r$, and $S = r$ can be seen in figure 43. The TCM plot of a single sphere is also included. Note that the energy scales are not the same in all the figures.

In the case of a single sphere, in figure 43d, the strongest contribution to the largest peak comes from transition 1p→1d. Another quite strong contribution comes from the transition 1p→2d. Other, smaller contributions are caused by transitions 1s→2p, 1p→2s, and transitions from 1p to states higher than 4 eV in energy.

The 1p→1d transition is also present in systems with separations of $S = 0.5r$ and $S = r$. However, in these systems it is weaker than the strongest transitions from 1p to the split 1f/2p states which are lower in energy than the 1f and 2p states in the single sphere. In

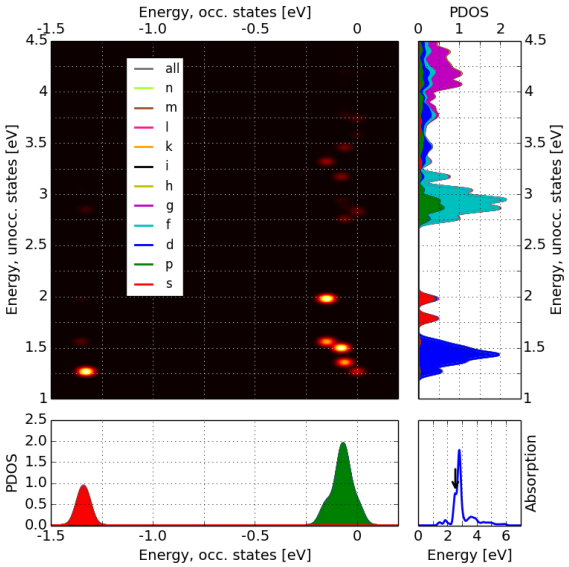

Figure 44: TCM plot of the second largest peak for the system with a separation of $S = 0.5r$. For details see the caption of figure 2.

the systems with two spheres there is also a contribution from the transition 1s→1d; this is especially strong in the systems with $S = 0.5r$ and $S = r$.

Apart from the transitions 1s→1d and 1p→1f/2p, the TCM of the system with $S = r$ is already quite close to the TCM of the single sphere. The TCM plot for the system with $S = 0.5r$, on the other hand, differs quite a lot from the single sphere TCM, and the TCM figure for the system with $S = 0$ is very different from that of the single sphere. In this cluster made of two spheres, contribution from the transition 1p→1d is very weak, and the strongest contributions come from transitions from 1p states to 1f/2p states. Here most of the transitions form a diagonal belt, as in the case of larger clusters, analysed in section 3.1.

In the system with $S = 0.5r$, the largest peak has a shoulder, a smaller peak adjacent to the largest peak. The TCM plot of this peak is displayed in figure 44. The TCM plot of this peak resembles more closely the TCM plot of the largest peak for the single sphere than the TCM of the largest peak, as there are strong contributions from the transitions 1p→1d. However, because of splitting of the states, the contribution from 1p→2s is much stronger than in the case of a single sphere, and there are transitions from 1s to 1d and 1d, which are not present in the case of a single sphere.

The TCM plots for the largest absorption peaks for the systems with $S = 1.5r$, $S = 2r$, $S = 3r$, and $S = 4r$ are presented in figure 43. When compared to figure 43d, it can be seen that the transitions in all these systems are already very close to the transitions in the case of a single sphere. The only clear difference is the transition 1s→1d in the system with $S = 1.5r$. Also, the transition 1s→2p is weaker in the systems with two spheres than in the case of a single sphere. However, looking at the transitions, the spectra and the electron states, when the separation between the two spheres is about 1.5–2 times the radius of the spheres, the optical response of the system is very similar to that of an isolated sphere.

The TCM plots of the small peak around 2 eV for the systems with separations $S = 0$,

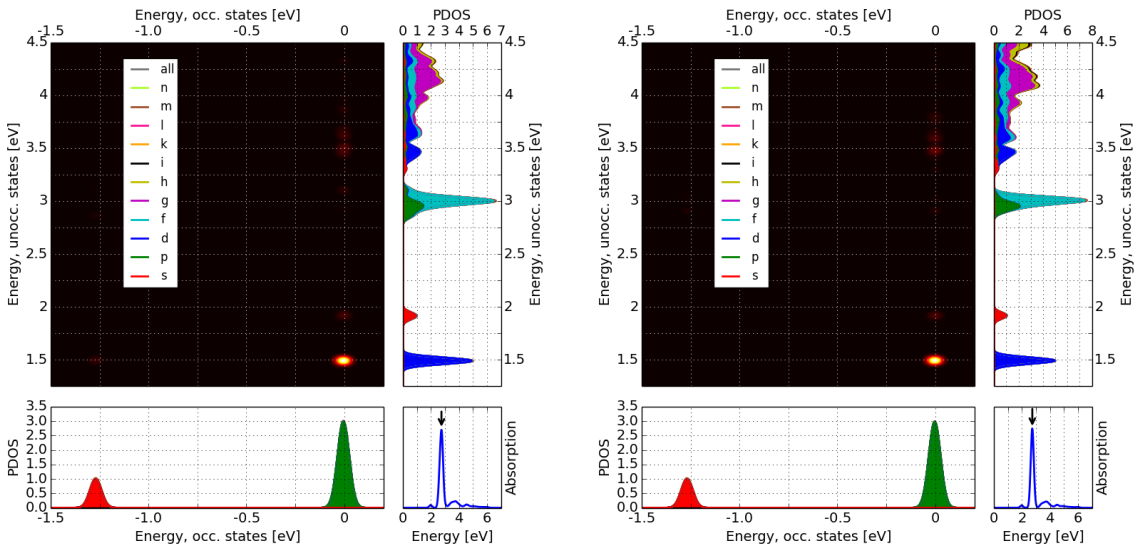

(a) $S = 1.5r$ **(b)** $S = 2r$

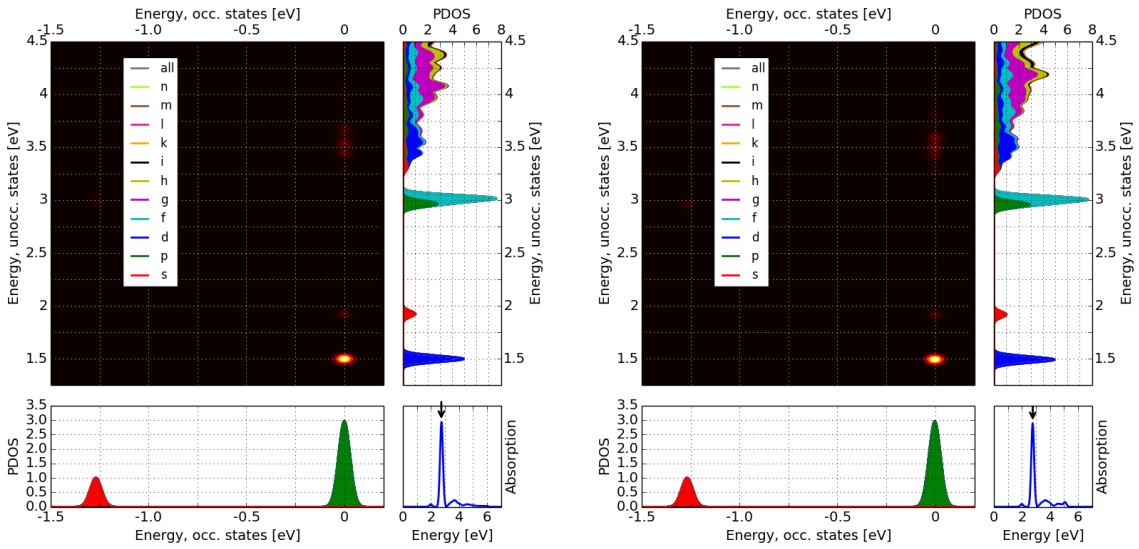

(c) $S = 3r$ **(d)** $S = 4r$

Figure 45: TCM plots for the largest peak for the systems of two Na_8 jellium spheres with separations $S = 1.5r$, $S = 2r$, $S = 3r$, and $S = 4r$. Note that the scales are not necessarily same in all the figures. For details see the caption of figure 2.

$S = 0.5r$, and $S = r$ and for the single sphere can be seen in figure 46. The energy of this peak is 1.75 eV for the system with $S = 0$, 1.86 eV for $S = 0.5r$, 1.96 eV for $S = r$, and 1.98 eV for the systems of larger separations and for the single sphere. For the single sphere, the main contribution comes from the transition 1p→2s. There is also a very weak contribution from the transition 1p→1d, but the peak can be thought of as being caused by a molecular, single-electron transition.

For the two spheres touching each other ($S = 0$) in figure 46a, the main transitions present are also 1p→2s and 1p→1d. However, because the states are split compared to the case of a single sphere, there are three transitions from 1p to 1d states and one from a 1p state to a 2s state. There are also some very weak contributions from transitions from 1p states

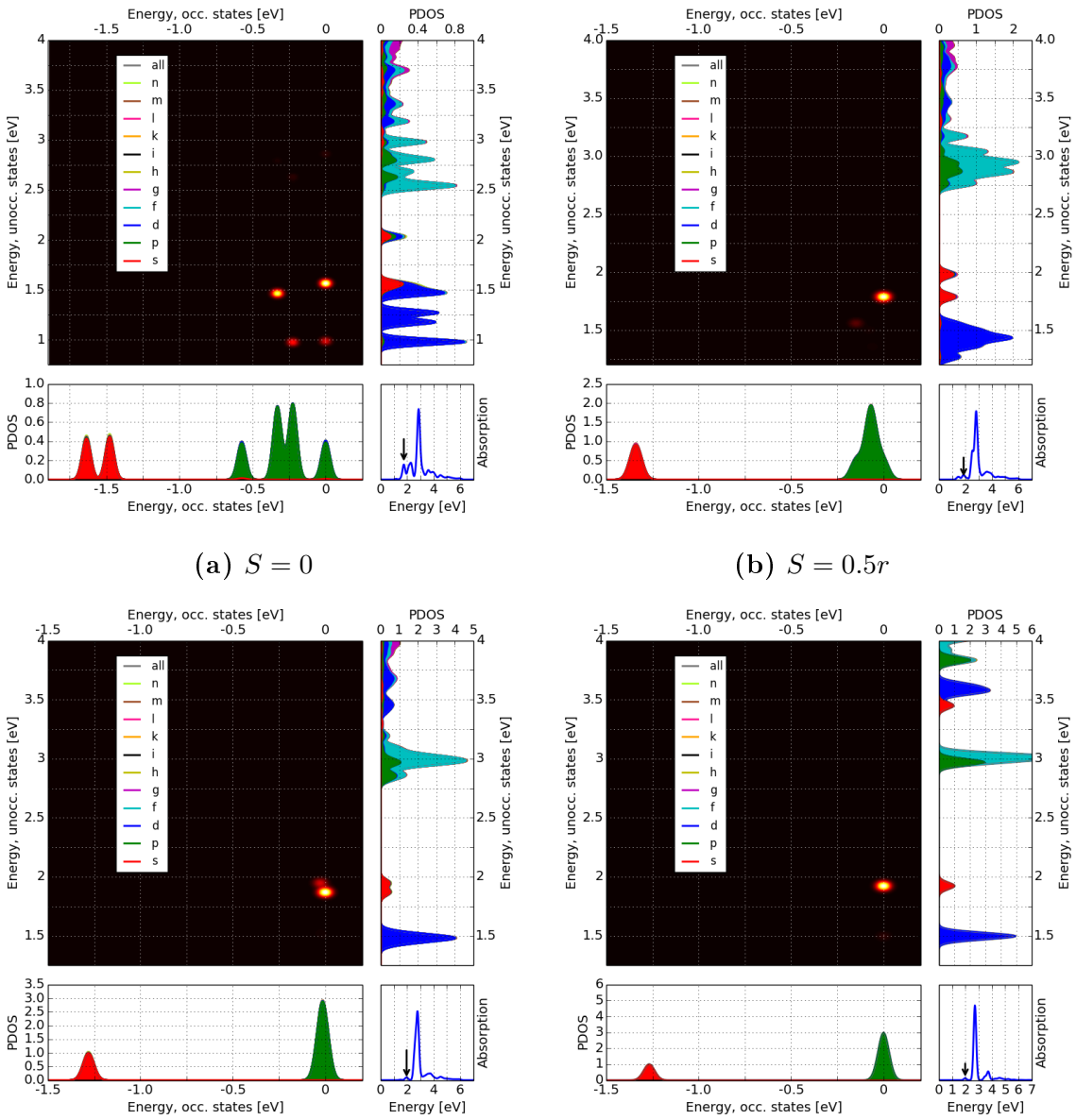

(a) $S = 0$ **(b)** $S = 0.5r$

(c) $S = r$ **(d)** single sphere

Figure 46: TCM plots of the small peak around 2 eV for the systems of two jellium spheres with eight atoms with separations $S = 0$, $S = 0.5r$, and $S = r$. The TCM plot of a single sphere is also included. Note that the energy scales are not necessarily same in all the figures. For details see the caption of figure 2.

to 1f/2p states.

In the system with separation $S = 0.5r$, the 1p, 1d and 2s states are still split compared to the states of a single sphere, but there are only two contributions: the main one from 1p→2s and a weaker from 1p→1d as in the case of a single sphere. For the system $S = r$ the states are still somewhat split, and there are two contributions from transitions 1p→2s. The transition 1p→1d is present, but very weak, and it cannot be clearly seen in figure 46c.

The systems with a separation of $1.5r$ or larger have TCM plots practically identical to that of a single sphere, seen in figure 46d.

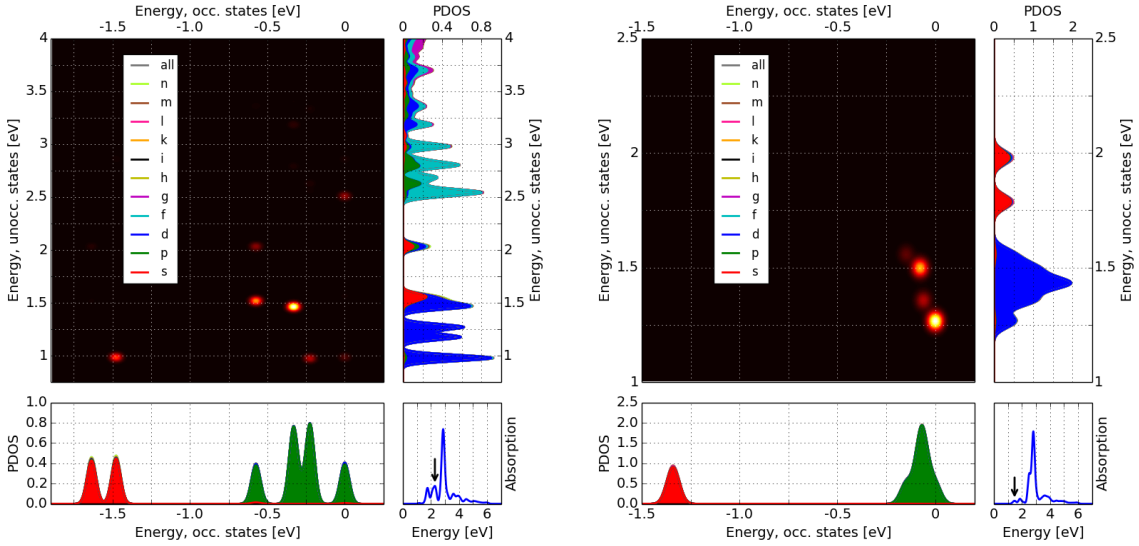

(a) $S = 0$ **(b)** $S = 0.5r$

Figure 47: TCM plots of the second peak for the system with $S = 0$ and the first peak for the system $S = 0.5r$. Note that the energy scales are not the same in the figures. For details see the caption of figure 2.

The systems with $S = 0$ and $S = 0.5r$ both had two smaller peaks before the largest peak or peaks. The first of these for the $S = 0$ system and the second for the $S = 0.5r$ system correspond to the first peak in the other systems, and their TCM plots are shown in figure 46d. The other peaks are displayed in figure 47.

Many transition contribute to the peak of figure 47a: 1s→1d, 1p→1d, 1p→2s, and 1p→1f. There are three transitions in a diagonal line across the plot, meaning all these transitions are of same energy (about 2.5 eV). The transitions from 1p states to 1d states and the lower 2s state are of smaller energy. Transitions from 1p states to 1d states cause the smallest peak in the spectrum of the system with $S = 0.5r$, as can be seen from figure 47b.

The induced densities for the largest peak for all the studied systems with two Na_8 spheres can be seen in figure 48. The induced density for a single sphere is also shown for comparison. All the figures 48a–48h are in different length scales. As can be seen, when the separation is $1.5r$ or larger, seen in figures 48d–48g, the induced densities of the individual spheres do not significantly differ from the induced density of a single sphere, seen in figure 48h.

Only the positive parts of the induced densities of figure 48 are presented in figure 49. The white dots show the jellium edges of the spheres. The negative parts are symmetric with respect to the positive parts, so they are not shown here separately.

The positive parts of the adjacent spheres differ from each other noticeably only in the systems with $S = 0$, $S = 0.5r$, and $S = r$. In systems with larger separations there are two shells of positive and negative density inside each sphere. These shells are approximately semispheres in shape. The single sphere also has such shells of induced density.

The induced densities have also been plotted radially along the axis that connects the two spheres, the x axis in the figures. These radial plots for the largest peaks can be seen in

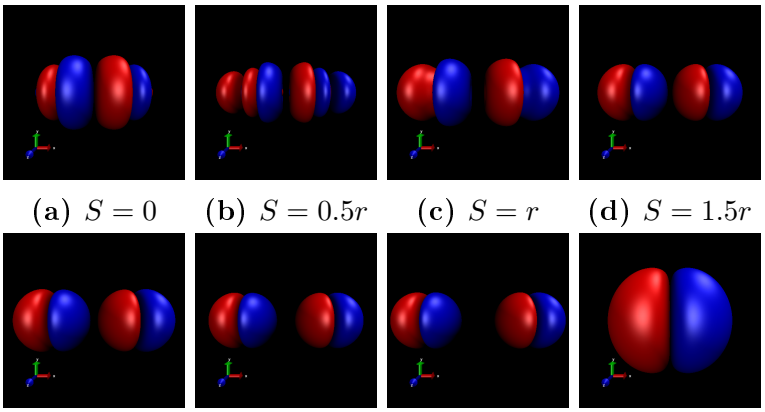

(a) $S = 0$ **(b)** $S = 0.5r$ **(c)** $S = r$ **(d)** $S = 1.5r$

(e) $S = 2r$ **(f)** $S = 3r$ **(g)** $S = 4r$ **(h)** single sphere

Figure 48: Induced densities for the largest peak for the systems of two Na_8 jellium spheres with separations $S = 0$, $S = 0.5r$, $S = r$, $S = 1.5r$, $S = 2r$, $S = 3r$, and $S = 4r$. The induced density of a single sphere is also included for comparison. The isosurface shown in red has the value of the jellium density, and the isosurface shown in blue has the value of the negative of the jellium density. All the figures are in different length scales.

figure 50 (systems with separations of 0, $0.5r$, r, and $1.5r$) and figure 51 (separations $2r$, $3r$, and $4r$, and a single sphere). Note that the density scales are different in figures 50 and 51.

The small systems with $S = 0$, $S = 0.5r$, and $S = r$ in figures 50a– 50c have more alternating layers of positive and negative density than the systems with larger separations. From $S = 1.5r$ onwards the shape of the radial plot does not change very much, as can be seen from figures 50d and 51a–51c. The inner shells of positive and negative density, the positive parts being in display in figures 48d–48g, are not seen in the radial plots for the systems with separations of $1.5r$, $2r$, $3r$, and $4r$. However, these layers of induced density can be seen in the radial plot for the single sphere in figure 51d. With separations larger than r, the densities inside the two spheres begin to be quite similar to each other, unlike in systems with $S = 0$, $S = 0.5r$, and $S = r$, where the induced densities of the left and right spheres are distinctly different from each other.

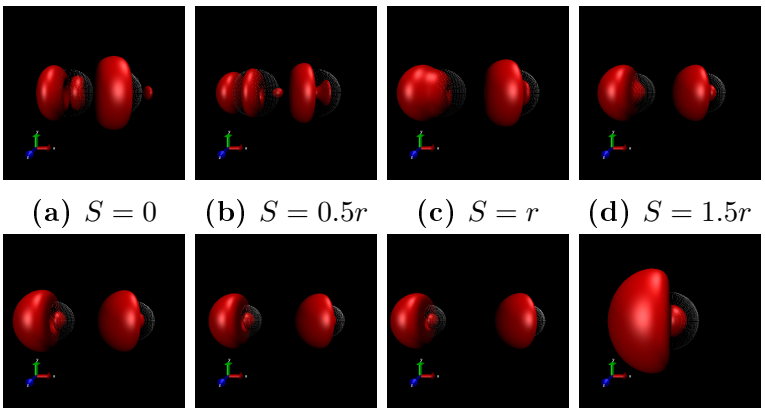

(a) $S = 0$ **(b)** $S = 0.5r$ **(c)** $S = r$ **(d)** $S = 1.5r$

(e) $S = 2r$ **(f)** $S = 3r$ **(g)** $S = 4r$ **(h)** single sphere

Figure 49: Only the positive parts of the induced densities of figure 48. The white spheres plotted with dots show the jellium edges of the spheres. All the figures are in different length scales.

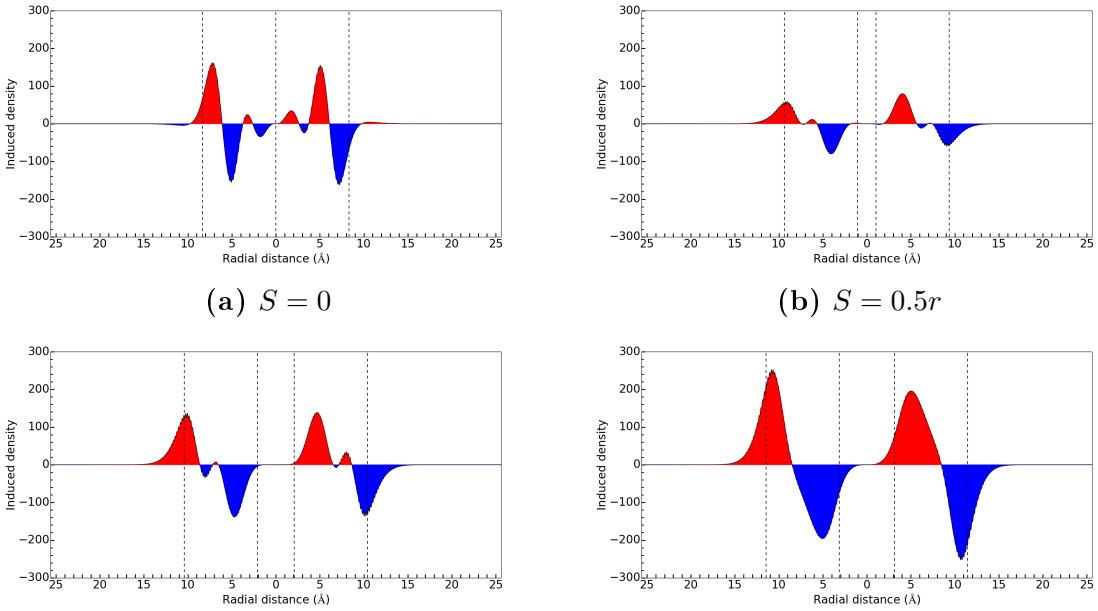

(a) $S = 0$ **(b)** $S = 0.5r$

(c) $S = r$ **(d)** $S = 1.5r$

Figure 50: Induced densities from figure 48 plotted radially for the systems with separations $S = 0$, $S = 0.5r$, $S = r$, and $S = 1.5r$. The radial axis is the axis connecting the two spheres. Positive density is indicated with red and negative with blue. The dashed verticals lines show the edges of the jellium spheres.

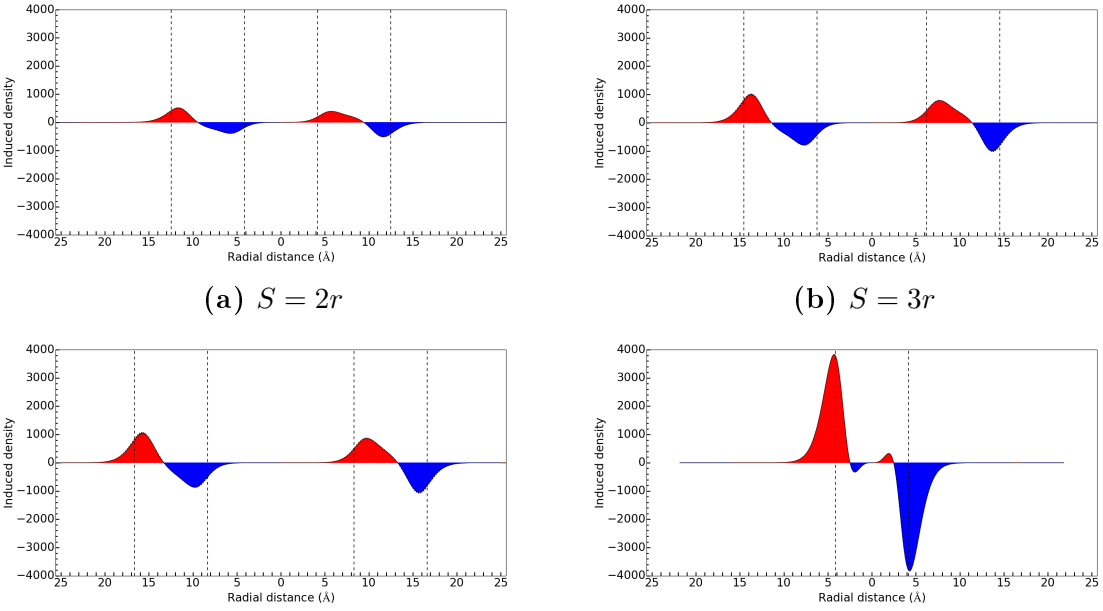

(a) $S = 2r$ **(b)** $S = 3r$

(c) $S = 4r$ **(d)** single sphere

Figure 51: Induced densities from figure 48 plotted radially for the systems with separations $S = 2r$, $S = 3r$, and $S = 4r$. The induced density of the corresponding peak for a single sphere is included for comparison. Note that the density scale is not the same as in figure 50. See the caption of figure 50 for other details.

As can be seen from figures 48b and 50b, the induced density for the largest peak for the system with $S = 0.5r$ differs somewhat from the induced densities of the largest peaks

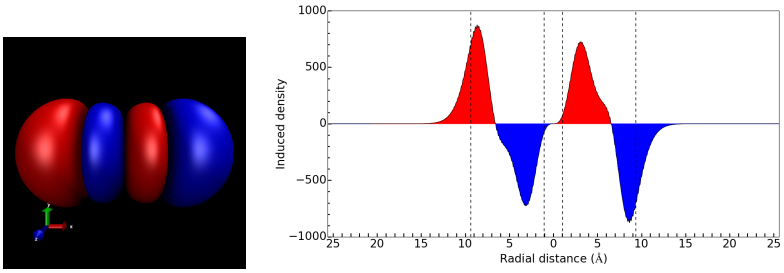

(a) **(b)**

Figure 52: Induced density for the second largest peak for the system with $S = 0.5r$. In figure 52a are depicted the isosurfaces of the induced density at the jellium density (red) and the negative of the jellium density (blue) visualised with VMD. In figure 52b is the induced density plotted radially along the axis connecting the two spheres.

for the other systems. In figure 52 are shown the isosurface of the induced density (figure 52a) and the radial plot of this density (figure 52b) of the second largest peak for the $S = 0.5r$ system. The induced density of this second largest peak is clearly closer to the induced density of the largest peak of the other systems. So, based on these induced densities and the TCM figures of the largest (figure 43b) and second largest (figure 44) peak for this system, of these two peaks the second largest peak resembles more closely the largest peak of the other systems.

In figure 53 are displayed the induced densities for the small peak at about 2 eV for the systems with $S = 0$, $S = 0.5r$, and $S = r$, and for a single sphere. Here already for $S = r$ the induced density in both spheres is very similar to that in the single sphere. This can be seen better by looking at the induced densities plotted radially, shown in figure 54. In systems with $S = r$ and $S = 1.5r$ there are two positive and two negative shells inside each sphere, as with the single sphere. The induced densities of systems with separations larger than 1.5r did not differ significantly from the induced density for the system with $S = 1.5r$.

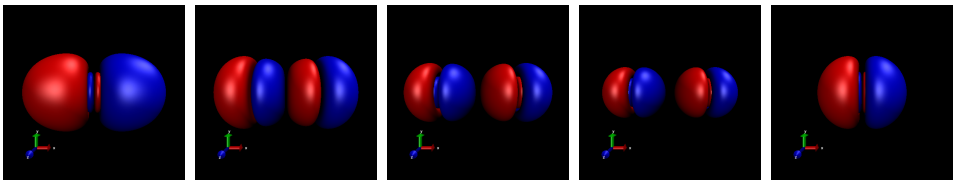

(a) $S = 0$ **(b)** $S = 0.5r$ **(c)** $S = r$ **(d)** $S = 1.5r$ **(e)** single sphere

Figure 53: Induced densities for the small peak at about 2 eV for the systems with separations $S = 0$, $S = 0.5r$, $S = r$, and $S = 1.5r$ All the figures are in different length scales. See the caption of figure 48 for details.

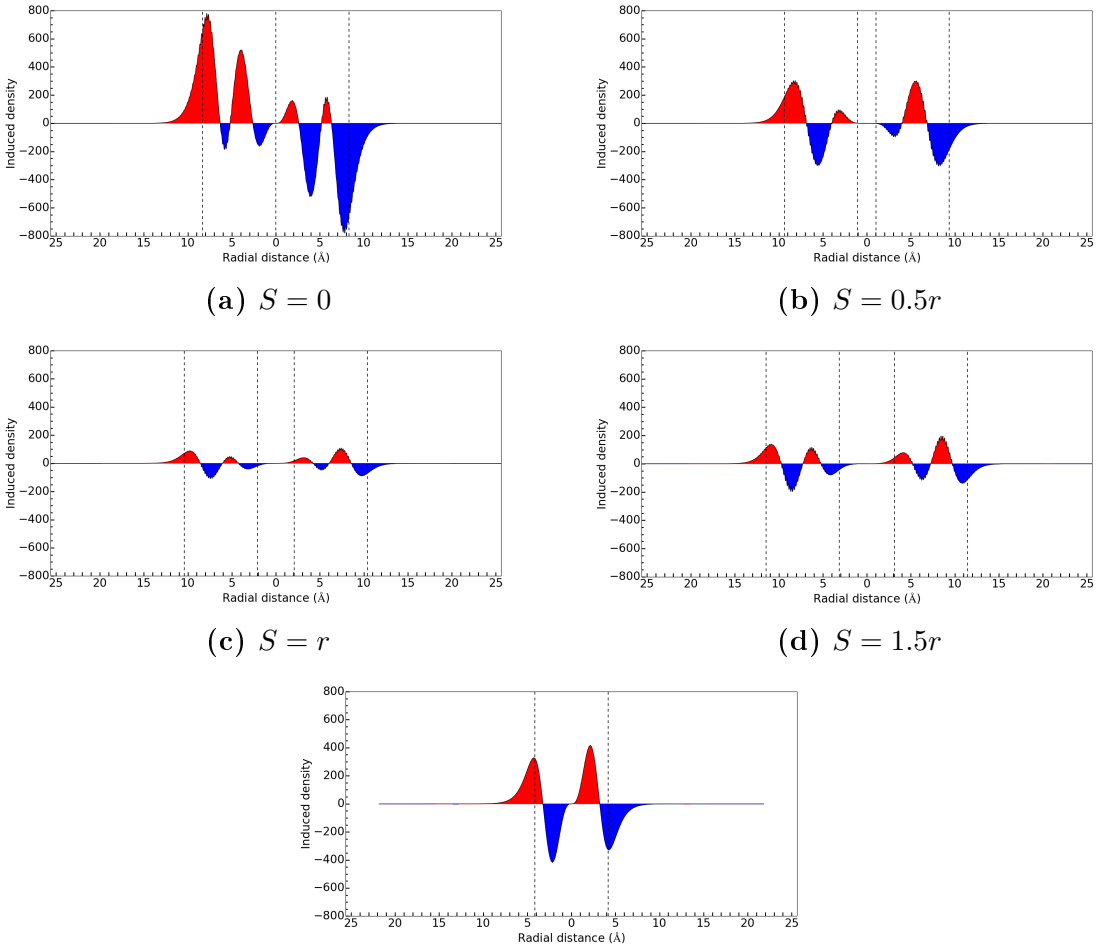

(a) $S = 0$

(b) $S = 0.5r$

(c) $S = r$

(d) $S = 1.5r$

(e) single sphere

Figure 54: Induced densities from figure 53 plotted radially for the systems with separations $S = 0$, $S = 0.5r$, $S = r$, and $S = 1.5r$. The induced density of a single sphere for the corresponding peak is included for comparison. See the caption of figure 50 for other details.

3.3.1 Largest peak for the $S = r$ system

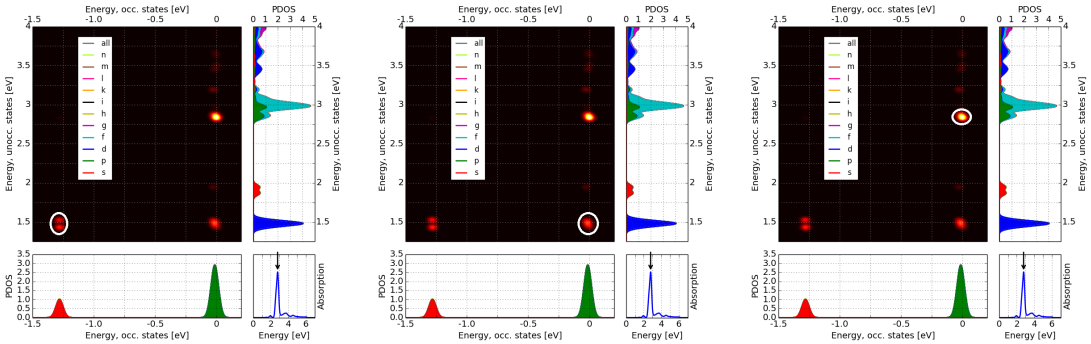

(a) 1s→1d **(b)** 1p→1d **(c)** 1p→1f

Figure 55: The analysed transitions are shown here circled in white.

The three strongest contributions for the largest peak for the system with $S = r$ were studied more: the induced densities were visualised with VMD and plotted radially for these three peaks separately. The studied contributions are marked in the TCM plot in figure 55.

The isosurfaces of the induced densities for each contribution can be seen in figure 56. The induced density from all the contributions is also included. In figure 57 is shown the induced density caused by the transition 1s→1d with three different isosurface values, because there is some structure at smaller density that can not be seen in figure 56b.

The radial plots of the induced densities seen in figure 56 are displayed in figure 58. From figures 56 and 58 it is clear that the transition 1p→1d causes most of the shape of the induced density. The deviation of the induced density of the peak from this shape of half-spheres is mostly caused by the transition 1p→1f. The induced density from transition 1p→1d is almost the same for both spheres, so the transitions are probably mainly between the states of each sphere separately, whereas the induced densities from transitions 1s→1d and 1p→1f are different between the two spheres.

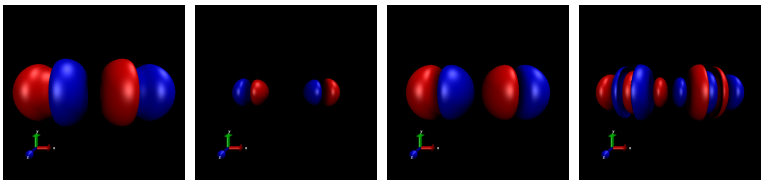

(a) all transitions **(b)** 1s→1d **(c)** 1p→1d **(d)** 1p→1f

Figure 56: The induced densities separately for the different transitions. In figure 56a is displayed the induced density for all the transitions contributing to the largest peak. In figures 56b, 56c, and 56d are the induced densities for the transitions shown in figure 55: 1s→1d, 1p→1d, and 1p→1f, respectively. The isosurface value of the red surface is the jellium density and the isosurface value for the blue surface is the negative of the jellium density. All the figures are in the same length scale.

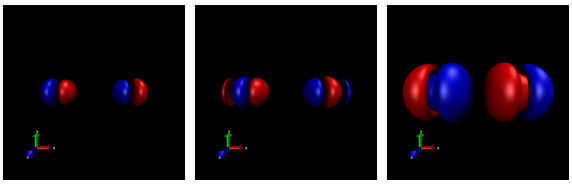

(a) jellium density

(b) half of jellium density

(c) one tenth of jellium density

Figure 57: The induced density for the transition 1s→1d for different isosurface values. In figure 57a the isosurface value is the jellium density (and its negative), in figure 57b it is half the jellium density and in figure 57c it is one tenth of the jellium density. All the figures are in the same length scale.

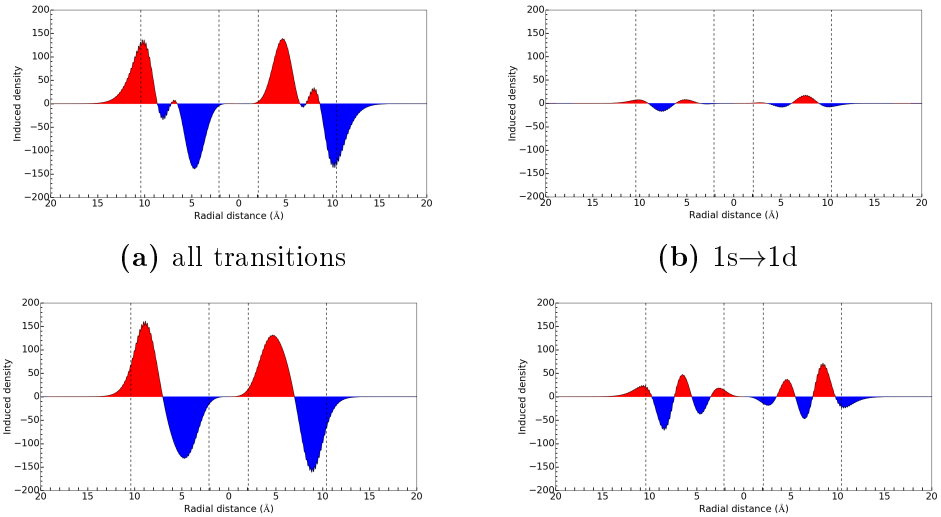

(a) all transitions

(b) 1s→1d

(c) 1p→1d

(d) 1p→1f

Figure 58: Radial plots of the induced densities from figure 56. The vertical dashed lines indicate the edges of the jellium spheres.

4 CONCLUSIONS

Different effects of the shape, size and arrangement of metal clusters on the optical properties of the system were observed in this study. The homogeneous jellium model with lr-TDDFT was used. With single jellium spheres, the intensity and position of the largest absorption peak changed when the size of the cluster changed. The obtained spectra were similar to spectra of jellium studies of Guet and Johnson [28] and Yannouleas et al. [29]. The transitions contributing to the largest peaks were studied using TD-DFTP. TCM analysis showed that all the studied absorption peaks were caused by many simultaneous single-electron transition. In the case of the Na_{40} jellium cluster, there were two large absorption peaks, which can be seen as a split plasmon peak. For the cluster with 58 electrons there were two large absorption peak close in energy, but one of these was clearly larger and caused by a more collective transition. In the spectra of the clusters with 92 and 138 electrons there was only one large absorption peak. The collective transitions and the fact that most of the electron density oscillation is concentrated on the surface of the clusters support the notion that these are LSPR peaks. The energy of these peaks seems to approach the LSPR limit for bulk-sized clusters, but bigger clusters should be studied to make any predictions about when the bulk limit will be achieved.

In the case of the two adjacent 8-electron spheres, the presence of the other cluster was observed to noticeably affect the shape of the optical spectrum only for clusters that are very close to each other, i.e. for separations of the length of the radius (4.16 Å) and smaller. However, the energy and intensity of the largest absorption peak did depend on the separation for all the systems studied, i.e. with separations up to 16.64 Å, which is four times the length of the radius of the clusters. This is in agreement with the results of Zuloaga et al. for two spherical jellium nanoparticles. The shape of the energy of the peak versus separation graph is also similar to the one from the article of Zuloaga et al.: when the separation between the clusters increases, the energy of the largest absorption peak first decreases and then starts to increase. The change in energy in relation to separation is slower for larger clusters, where the peak energy is getting bigger. However, the separation where the energy of the largest peak is at minimum is much larger in this study than in the study of Zuloaga et al., both in absolute length and in separation versus radius ratio. This might be explained by the different jellium densities used or the different sizes of the clusters: in the study of Zuloaga et al., the smallest clusters had 302 free electrons, a radius of 8.46 Å, and a Wigner-Seitz radius of 1.59 Å; here the clusters had 8 electrons, a radius of 4.16 Å, and a Wigner-Seitz radius of 2.08 Å. Clusters with more electrons or with a smaller Wigner-Seitz radius should be studied to see if the density or size of the clusters or both affect the location of the minimum peak energy.

The effect of shape was studied by comparing the spherical 138-electron cluster to a cluster with the same amount of electrons but in the shape of a cuboctahedron. The change in shape could be observed in the optical spectrum, transitions contributing to the plasmon peak, and induced density for the plasmon peak. This was due to splitting of states in the Na_{138} jellium cuboctahedron compared to the Na_{138} jellium sphere, which caused the cuboctahedron to have a more collective plasmon peak.

The homogeneous jellium model used here is very simple in that it does not take the ion structure of the clusters into account. Also, jellium models cannot be used to study systems with ligands, which are used in many applications, as mentioned in the introduction. For more realistic approximations, inhomogeneous jellium models or atomistic models should be used. The calculation methods used in this study are suitable also for atomistic calculations, and have been used for calculating the optical properties of ligand-covered gold clusters [17], [50].

REFERENCES

[1] I. Freestone et al. The Lycurgus Cup - A Roman nanotechnology. *Gold Bulletin* **40** (2007) 270–277. **DOI**: 10.1007/BF03215599

[2] M. Faraday. The Bakerian lecture: Experimental relations of gold (and other metals) to light. *Philosophical Transactions of the Royal Society of London* **147** (1857) 145–181. Downloaded from http://rstl.ryalsocietypublishing.org/ on June 4, 2015.

[3] G. Mie. Beiträge zur Optik trüber Medien, speziell kolloidaler Metallösungen. *Annalen der Physik* **330** (1908) 377–445. **DOI**: 10.1002/andp.19083300301

[4] J.J. Mock et al. Shape effects in plasmon resonance of individual colloidal silver nanoparticles. *The Journal of Chemical Physics* **116** (2002) 6755–6759. **DOI**: 10.1063/1.1462610

[5] S. Link and M. El-Sayed. Size and temperature dependence of the plasmon absorption of colloidal gold nanoparticles. *The Journal of Physical Chemistry B* **103** (1999) 4212–4217. **DOI**: 10.1021/jp984796o

[6] K. Selby et all. Photoabsorption spectra of sodium clusters. *Physical Review B* **43** (1991) 4565 –4572. **DOI**: 10.1103/PhysRevB.43.4565

[7] K.-H. Su et al. Interparticle coupling effects on plasmon resonances of nanogold particles *Nano Letters* **3** (2003) 1087–1090. **DOI**: 10.1021/nl034197f

[8] C. Sönnichsen et al. A molecular ruler based on plasmon coupling of single gold and silver nanoparticles. *Nature Biotechnology* **23** (2005) 741–745. **DOI**: 10.1038/nbt1100

[9] K.L. Kelly et al. The optical properties of metal nanoparticles: the influence of size, shape, and dielectric environment. *The Journal of Physical Chemistry B* **107** (2003) 668 –677. **DOI**:10.1021/jp026731y

[10] A.J. Hayes and R.P. Van Duyne. A nanoscale optical biosensor: sensitivity and selectivity of an approach based on the localized surface plasmon resonance spectroscopy of triangular silver nanoparticles *Journal of the American Chemical Society* **124** (2002) 10596–10604. **DOI**: 10.1021/ja020393x

[11] K.A. Willets and R.P. Van Duyne. Localized surface plasmon resonance spectroscopy and sensing *Annual Review of Physical Chemistry* **58** (2007) 267–297. **DOI**: 10.1146/annurev.physchem.58.032806.104607

[12] N.J. Halas et al. Plasmons in strongly coupled metallic nanostructures *Chemical Reviews* **111** (2011) 3913–3961. **DOI**: 10.1021/cr200061k

[13] X. Huang et al. Cancer cell imaging and photothermal therapy in the near-infrared region by using gold nanorods *Journal of the American Chemical Society* **128** (2006) 2115–2120. **DOI**: 10.1021/ja057254a

[14] I.H. El-Sayed, X. Huang, and M-A. El-Sayed. Selective laser photo-thermal therapy of epithelial carcinoma using anti-EGFR antibody conjugated gold nanoparticles *Cancer Letters* **239** (2006) 129–135.**DOI**: 10.1016/j.canlet.2005.07.035

[15] J.J. Mortensen, L. B. Hansen, and K. W. Jacobsen. Real-space grid implementation of the projector augmented wave method. *Physical Review B* **71** (2005) 035109-1–035109-11. **DOI**: 10.1103/PhysRevB.71.035109.

[16] J. Enkovaara et al. Electronic structure calculations with GPAW: a real-space implementation of the projector augmented-wave method. *Journal of Physics: Condensed Matter* **22** (2010) 1–24. **DOI**: 10.1088/0953-8984/22/25/253202

[17] S. Malola et al. Birth of the localized surface plasmon resonance in monolayer-protected gold nanoclusters. *ACS Nano* **7** (2013) 10263–10270 . **DOI**: 10.1021/nn4046634

[18] M. Brack. The physics of simple metal clusters: self-consistent jellium model and semiclassical approaches. *Reviews of modern physics* **65** (1993) 677–732. **DOI**: 10.1103/RevModPhys.65.677

[19] E.B. Guidez and C.M. Aikens. Quantum mechanical origin of the plasmon: from molecular systems to nanoparticles. *Nanoscale* **6** (2014) 11512 –11527. **DOI**: 10.1039/c4nr02225d

[20] S. Raza et al. Unusual resonances in nanoplasmonic structures due to nonlocal response. *Physical Review B* **84** (2011) 121412-1–121412-4 . **DOI**: 10.1103/PhysRevB.84.121412

[21] W. Yang, G. Schaz, and R. Duyne. Discrete dipole approximation for calculating extinction and Raman intensities for small particles with arbitrary shapes. *The Journal of Chemical Physics* **103** (1995) 869–875. **DOI**: 10.1063/1.469787

[22] K.S. Yee. Numerical solution of initial boundary value problems involving Maxwell's equations in isotropic media. *IEEE Transactions on Antennas and Propagation* **14** (1966) 30 –307. **DOI**: 10.1109/TAP.1966.1138693

[23] R. Esteban et al. Bridging quantum and classical plasmonics with a quantum-corrected model. *Nature Communications* **3** (2012) 825 **DOI**: 10.1038/ncomms1806

[24] E. Prodan et al. A hybridization model for the plasmon response of complex nanostructures. *Science* **302** (2003) 419–422. **DOI**: 0.1126/science.1089171

[25] P. Nordlander et al. Plasmon hybridization in nanoparticle dimers. *Nano Letters* **4** (2004) 899–903. **DOI**: 10.1021/nl049681c

[26] E. Runge and EK.U. Gross. Density-functional theory for time-dependent systems. *Physical Review Letters* **52** (1984) 997–1000. **DOI**: 10.1103/PhysRevLett.52.997

[27] J.P. Perdew and Y. Wang. Accurate and simple analytic representation of the electron-gas correlation energy. *Physical Review B* **45** (1992) 13 244 – 13 249. **DOI**: 10.1103/PhysRevB.45.13244

[28] C. Guet and W.R. Johnson. Dipole excitations of closed-shell alkali-metal clusters. *Physical Review B* **45** (1992) 11 283–11 287. **DOI**: 10.1103/PhysRevB.45.11283

[29] C. Yannouleas, E. Vigezzi, and R.A. Broglia. Evolution of the optical properties of alkali-metal microclusters towards the bulk: The matrix random-phase approximation description. *Physical Review B* **47** (1993) 9849–9861. **DOI**: 10.1103/PhysRevB.47.9849

[30] J. Zuloaga, E. Prodan, and P. Nordlander. Quantum description of the plasmon resonances of a nanoparticle dimer. *Nano Letters* **9** (2009) 887–891. **DOI**: 10.1021/nl803811g

[31] W. Ekardt. Work function of small metal particles: Self-consistent spherical jellium-background model. *Physical Review B* **29** (1984) 1558–1564. **DOI**: 10.1103/PhysRevB.29.1558

[32] T.V. Teperik et al. Quantum effects and nonlocality in strongly coupled plasmonic nanowire dimers. *Optics Express* **21** (2013) 27306–27325. **DOI**: 10.1364/OE.21.027306

[33] E. Prodan and P. Nordlander. Structural tunability of the plasmon resonances in metallic nanoshells. *Nano Letters* **3** (2003) 543–547. **DOI**: 10.1021/nl034030m

[34] P. Zhang et al. Ab initio nanoplasmonics: The impact of atomic structure. *Physical Review B* **90** (2014) 161407-1–161407-5. **DOI**: 10.1103/PhysRevB.90.161407

[35] T. Lange et al. Calculated electronic properties of medium sized sodium clusters - the inhomogeneous jellium model. *Zeitschrift für Physik D* **19** (1991) 113–115. **DOI**: 10.1007/BF01448268

[36] M. Koskinen, P.O. Lipas ja M. Manninen. Electron-gas clusters: the ultimate jellium model. *Zeitschrift für Physik D* **35** (1995) 285–297. **DOI** 10.1007/BF01745532

[37] S. Link and M. El-Sayed. Shape adjustment between multiply twinned and single-crystalline polyhedral gold nanocrystals: decahedra, icosahedra, and truncated tetrahedra. *The Journal of Physical Chemistry C* **112** (2008) 2469–2475. **DOI**: 10.1021/jp7109498

[38] W. Ekardt and Z. Penzar. Collective excitations in open-shell metal clusters: The time-dependent local-density approximation applied to the self-consistent spheroidal jellium. *Physical Review B* **43** (1991) 1322–1330. **DOI**: 10.1103/PhysRevB.43.1322

[39] S. Pollack, C. Wang, and M. Kappes. On the optical response of Na_{20} and its relation to computational prediction. *The Journal of Chemical Physics* **94** (1991) 2496–2501. **DOI**: 10.1063/1.459873

[40] C. Yannouleas and E. Vigezzi. Evolution of the optical properties of alkali-metal microclusters towards the bulk: The matrix random-phase approximation description. *Physical Review B* **47** (1993) 9849–9861. **DOI**: 10.1103/PhysRevB.47.9849

[41] A. Rubio, L.C. Balbás, and J.A. Alonso. Influence of nonlocal exchange-correlation effects on the response properties of simple metal clusters. *Physical Review B* **46** (1992) 4891–4898 **DOI**: 10.1103/PhysRevB.46.4891

[42] H. Yin and H. Zhang. Quantum mechanical study of plasmonic coupling in sodium nanoring dimers. *Applied Physics Letters* **101** (2012) 061906-1–061906-5 **DOI**: 10.1063/1.4745654

[43] C. Tabor, D. Van Haute, and M.A. El-Sayed. Effect of orientation on plasmonic coupling between gold nanorods. *ACS Nano* **3** (2009) 3670–3678 **DOI**: 10.1021/nn900779f

[44] S.R. Bahn and K.W. Jacobsen. An object-oriented scripting interface to a legacy electronic structure code. *Computing in Science & Engineering* **4** (2002) 55–66. **DOI**: 10.1109/5992.998641

[45] P.E. Blöchl. Projector augmented-wave method. *Physical Review B* **50** (1994) 17 953–17 979. **DOI**: 10.1103/PhysRevB.50.17953

[46] M. Walter et al. Time-dependent density-functional theory in the projector augmented-wave method. *The Journal of Chemical Physics* **128** (2008) 244101. **DOI**: 0.1063/1.2943138

[47] X. Andrade et al. Time-dependent density functional theory scheme for efficient calculations of dynamic (hyper)polarizabilities. *The Journal of Chemical Physics* **126** (2007) 184106. **DOI**: 10.1063/1.2733666

[48] W. Humphrey, A. Dalke and K. Schulten. VMD: Visual molecular dynamics. *Journal of Molecular Graphics and modelling* **14** (1996) 33–38. **DOI**: 10.1016/0263-7855(96)00018-5

[49] E. Selenius. Optical properties of jellium clusters Na_8 and Na_{20} using GPAW. Unpublished Research Study thesis. Department of Physics, University of Jyväskylä (2015).

[50] H. Yang et al. All-thiol-stabilized Ag_{44} and $Au_{12}Ag_{32}$ nanoparticles with single-crystal structure. *Nature Communications* **4** (2013) 2422 . **DOI**: 10.1038/ncomms3422